Growth and Characterization of Cobalt-doped $BaFe_2As_2$ Epitaxial Thin Films and Superlattices

By

Sanghan Lee

A dissertation submitted in partial fulfillment of

the requirements for the degree of

Doctor of Philosophy

(Materials Science Program)

at the

University of Wisconsin – Madison

2012

Date of final oral examination: July 26, 2012

The dissertation is approved by the following members of the Final Oral Committee:

Chang-Beom Eom, Professor, Materials Science and Engineering

John H. Perepezko, Professor, Materials Science and Engineering

Mark Rzchowski, Professor, Physics

Robert F. McDermott, Associate Professor, Physics

Eric E. Hellstrom, Professor, Mechanical Engineering

Abstract

The synthesis of high quality single crystal thin films and multilayers of pnictide superconductors is critical to explore their intrinsic properties and evaluate novel device applications. In this study, we have grown genuine epitaxial thin films of Co-doped $BaFe_2As_2$ (Ba-122) by employing template engineering. The epitaxial thin films on single-crystal (001) $SrTiO_3$ template on (001) LSAT substrates exhibit high transition temperature ($T_{c,\rho=0}$ of 21.5K), superior critical current density (J_c) of 4.5 MA/cm^2 (4.2K, self field) and strong *c*-axis flux pinning. We have also studied grain boundary (GB) characteristics of epitaxial Co-doped Ba-122 thin films on $SrTiO_3$ bicrystal substrates. Despite their low anisotropy ($H_{c2}^{(ab)}/H_{c2}^{(c)}<2$), strong vortex pinning and high irreversibility field (H_{irr}) close to upper critical field (H_{c2}) which is well over 50 T, the critical current density J_b across [001] tilt GBs of thin film Co-doped Ba-122 bicrystals is strongly depressed, exhibiting weak link GB behavior similar to high-T_c cuprates. Our results suggest that weak-linked GBs are characteristic of high-T_c superconducting compounds with competing orders, low carrier density, and unconventional pairing symmetry. Artificial layered pnictide superlattices offer unique opportunity towards tailoring superconducting properties and understanding the mechanisms of superconductivity by creating model structures which do not exist in nature. For high field applications, very high J_c and H_{irr} are indispensable along all crystal directions. On the other hand, the development of superconducting devices such as tunnel junctions requires multilayered heterostructures. We have demonstrated that artificially engineered undoped Ba-122 / Co-doped Ba-122 compositionally modulated superlattices produce *ab*-aligned nanoparticle arrays by layering and self-assembled *c*-axis

aligned defects that combine to produce very large J_c and H_{irr} enhancements over a wide angular range. We also demonstrate a structurally modulated $SrTiO_3$ (STO) / Co-doped Ba-122 superlattice with atomically sharp interfaces. The synthesis of the epitaxial pnictide thin films and artificial layered superlattices of pnictide superconductors opens many avenues for superconducting electronic device applications and for model experiment in superconductivity.

TABLE OF CONTENTS

Abstract ……...i

Chapter I. Introduction ……...1

I-1. Background...…….....1

I-2. Epitaxial thin film growth of iron-based superconductors…….....3

I-3. Grain Boundary characteristics of superconductors…….4

I-4. Artificial layered structures and their properties……..5

I-5. Effect of strain on the T_c of iron-based superconductor thin films……7

References…….....9

Chapter II. Experimental Setup……11

II-1. Pulsed laser deposition system……..11

II-2. X-ray diffraction measurement……13

II-3. Electrical transport and electromagnetic measurement…….14

References…….15

Chapter III. Template engineering of Co-doped $BaFe_2As_2$ single-crystal thin films…16

III-1. Scientific issue about the iron based superconductor growth……16

III-2. Template engineering using titanates oxide layer……16

III-3. Structural properties of Co-doped Ba-122 thin films……..20

III-4. Superconducting properties of Co-doped Ba-122 thin films……24

III-5. Summary of the chapter……...29

References…….32

Chapter IV. Weak link behavior of grain boundaries in Co-doped $BaFe_2As_2$……..33

IV-1. Scientific issue about grain boundaries in superconductors……33

IV-2. Epitaxial growth of Co-doped Ba-122 on STO bicrystal……34

IV-3. Structural properties of Co-doped Ba-122 grown on STO bicrystal……...35

IV-4. Evidences of weak link behavior in Co-doped Ba-122……...39

IV-5. Summary of the chapter……...47

References……48

Chapter V. Artificially engineered superlattices of Co-doped $BaFe_2As_2$…….....50

V-1. The growth of Co-doped Ba-122 superlattices……50

V-2. Crystalline quality of Co-doped Ba-122 superlattices…….....53

V-3. Microstructure of Co-doped Ba-122 superlattices……...55

V-4. Superconducting properties of Co-doped Ba-122 superlattices……...58

V-5. Summary of the chapter……62

References……63

Chapter VI. Strain effect on T_c of Co-doped $BaFe_2As_2$……65

VI-1. Thermal expansion mismatch between Co-doped Ba-122 and CaF_2…….……65

VI-2. Structural properties of Co-doped Ba-122 thin films grown on CaF_2 substrate.....67

VI-3. Superconducting properties of Co-doped Ba-122 thin films grown on CaF_2 substrate……70

VI-4. Summary of the chapter……...75

References……76

Chapter VII. Summary……...78

VII-1. Growth of genuine epitaxial Co-doped Ba-122 thin film and its properties of grain boundaries……..……...…78

VII-2. Tailoring superconducting properties by artificial layered superlattices and a strain effect……..79

APPENDIX; Dependence of epitaxial Co-doped $BaFe_2As_2$ thin films properties on $SrTiO_3$ template thickness …….81

References……92

Acknowledgement……...94

Chapter I. Introduction

I-1. Background

Since the discovery of superconductivity in Hg by Heike Kamerlingh Onnes in 1911 [1], significant progress has been made in, understanding the fundamental physics and improving their performances. Figure I.1 shows the discovery timeline of superconducting materials. In 2006, Hosono and his colleagues discovered superconductivity in the LaFePO system(so called "1111"), which has a T_c of ~4 K [2]. The scientific community referred to this new material system as an Fe-based superconductor (FeSC). Two years later, they discovered superconductivity at 26 K in F-doped LaFeAsO [3], which led to extensive studies.

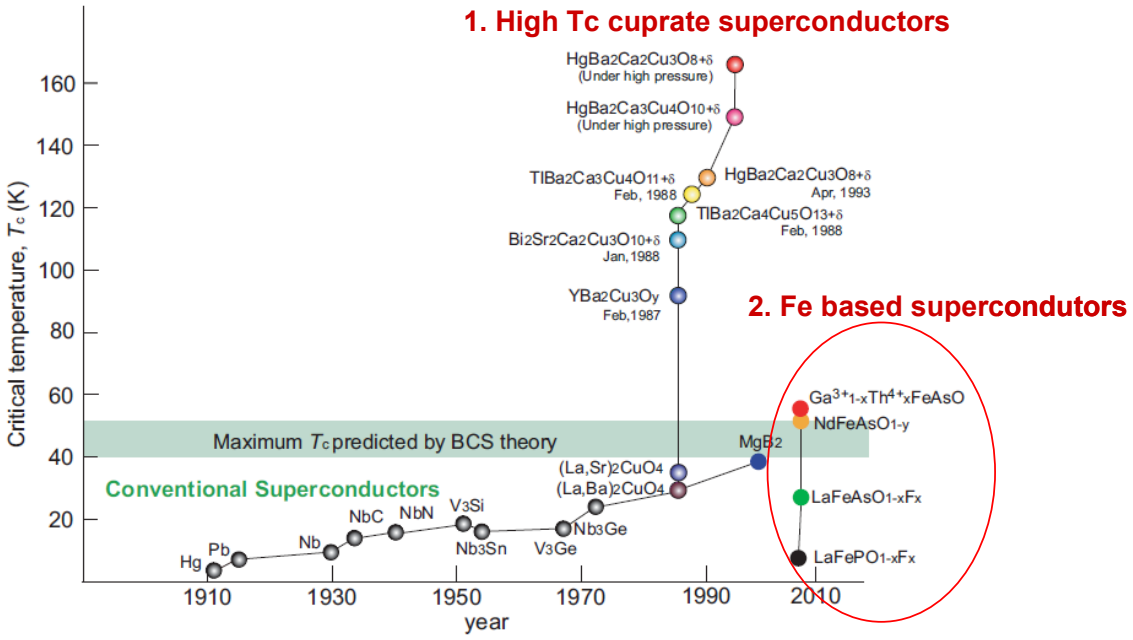

Figure I.1. Discovery timeline of superconductors. [7].

Chen and Wang reported superconductivity in other 1111 FeSC systems; F-doped SmFeAsO at ~43K [5] and Th-doped GdFeAsO at 56K [6]. Other types of FeSCs, aside from the 1111 structure, were also discovered. The $ThCr_2Si_2$ type 122 structure, which consists of alkaline earth (AE), Fe, and As, shows superconducting transitions at 38 K and 22 K with K- or Co-doping at the AE or Fe sites, respectively [8, 9]. CeFeSi-type AFeAs (A is alkali metal) phase (111 structure) [10] and anti-PbO-type FeSe phase (11 structure) [11] were also reported (Fig. I.2).

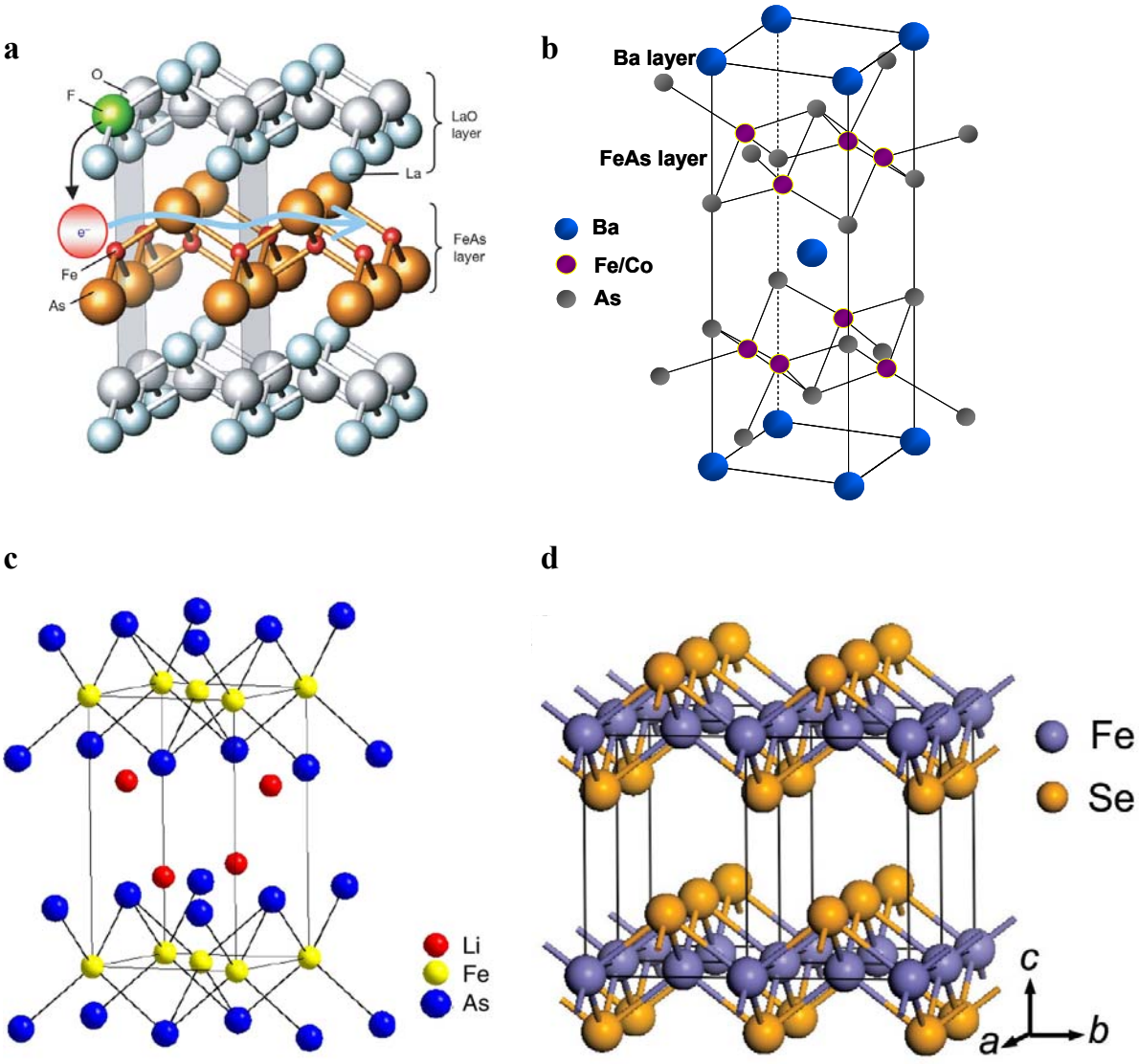

Figure I.2. Crystal structures of various iron-based superconductors.

a. F-doped LaFeAsO [3] b. Co-doped $BaFe_2As_2$ c. LiFeAs [10] and d. FeSe [11]

The ability to design and fabricate high quality epitaxial thin films of new superconducting materials is necessary to explore intrinsic electromagnetic properties and evaluate device applications. In this study, we grew epitaxial Co-doped $BaFe_2As_2$ (Ba-122) thin films and superlattices.

I-2. Epitaxial thin film growth of iron-based superconductors

Immediately after the discovery of the 1111 phase F-doped LaFeAsO superconductor [3], several research groups attempted to grow epitaxial thin films of the 1111 phase. Hiramatsu reported the growth of LaFeAsO epitaxial films on oxide substrates; however, superconductivity was not observed [12]. Haindl reported *ex-situ* annealed F-doped LaFeAsO thin films with superconducting properties, but the crystalline quality of the films were compromised [13]. The difficulty in growing high quality F-doped LaFeAsO epitaxial thin films is due to the volatile elements involved, such as F and As, which make it hard to control the stoichiometry during growth at high temperatures.

Co-doped AE (alkaline earth element, such as Ca, Sr, Ba)-122 systems are favorable because it is easy to control the Co content during the thin film growth. Several groups have reported the growth of epitaxial Co-doped Ba-122 thin films. However, the superconducting properties, such as superconducting transition widths (ΔT_c) and critical

current density (J_c), were still compromised in the early stages [14-16].

I-3. Grain boundary characteristics of superconductors

The discovery of any new high transition temperature T_c superconductor immediately poses the question of whether it has the essential qualities for applications: high critical current density J_c, high upper critical field H_{c2} and irreversibility field H_{irr}, and low anisotropy = $H_{c2}^{(ab)}/H_{c2}^{(c)}$. When the high T_c superconductor $YBa_2Cu_3O_{7-\delta}$ (YBCO) was discovered, the single crystal YBCO showed some potential in regard to these requirements. However, in polycrystalline YBCO, a low J_c, a few hundred A/cm^2 at 4.2 K, apparently ruled out the high field application. The J_c behaviors of polycrystalline high T_c superconductors are mainly determined by the grain boundaries [17]. To understand the J_c characteristics of bulk polycrystalline material, a well-defined individual grain boundary was needed [17]. To reveal the superconducting properties across the grain boundaries, the YBOC thin film bicrystals were developed [17].

Using the bicrystal approach, it was revealed that the low critical current density in polycrystalline YBCO is due to the high angle grain boundaries. High angle grain boundaries limit supercurrent and it results in a lower J_c, compared with intra-grain Jc as shown in Fig. I.3 [18]. Systematic studies of grain boundaries for unconventional FeSC are important to understand the superconductivity and explore the potential applications.. For this thesis, we studied grain boundary characteristics of epitaxial Co-doped Ba-122 thin films on (001) $SrTiO_3$ bicrystal substrates by varying the misorientation angles.

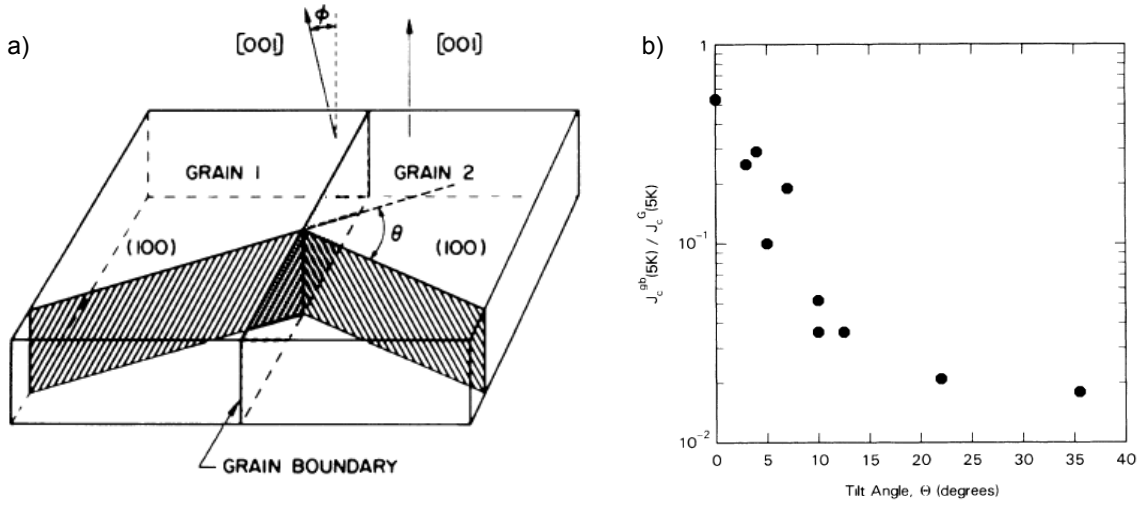

Figure I.3. Grain boundaries study on $YBa_2Cu_3O_{7-d}$ [18].

a. Schematic diagram showing the important crystallography of the SrTi03 bicrystals that were used as substrates for the thin-film deposition.

b. Plot of the ratio of the grain-boundary critical current density to the average value of the critical current density in the two grains at 4.2-5 K vs. the misorientation angle in the basal plane.

I-4. Artificial layered structures and their properties

Artificially layered thin film heterostructures are desirable to understand fundamental physics of new superconducting materials and discover novel interface phenomena [19-21]. Triscone et al. reported that a minimum interlayer coupling is necessary for superconductivity to occur in the individual thin YBCO layers using artificially layered YBCO/$PrBa_2Cu_3O_7$ (PBCO) superlattices, as shown in Fig. I.4a [19].

Additionally, Gozar discovered superconductivity in bilayers consisting of an insulator (La_2CuO_4) and a metal ($La_{1.55}Sr_{0.45}CuO_4$), as shown in Fig. I.4b [21].

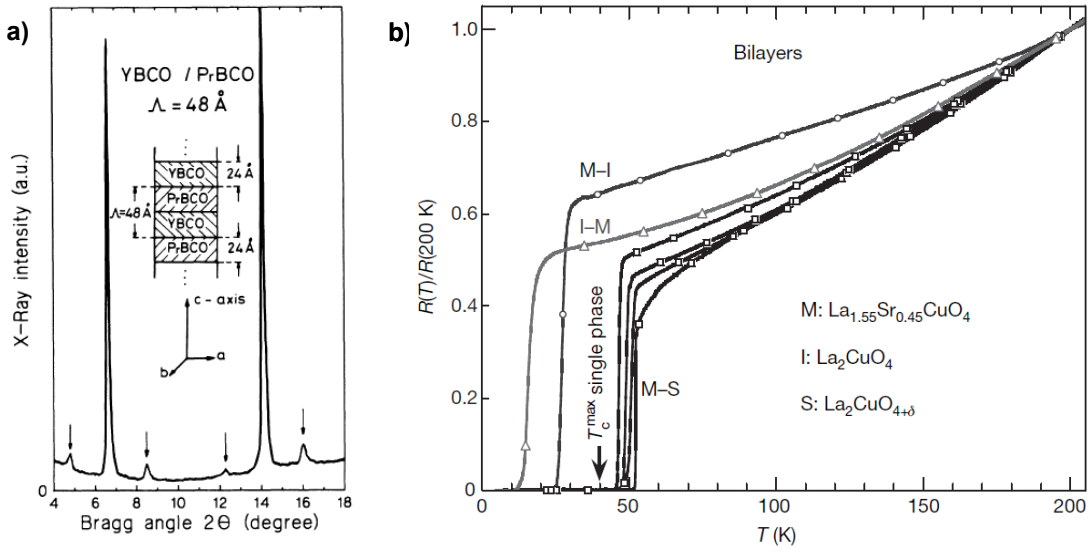

Figure I.4. Structural and electromagnetic properties of unique superconducting heterostructures.

a. θ-2θ x-ray diffractogram of a Λ = 48 Å (24-Å/24-Å) YBCO/PBCO multilayer. The satellite peaks are indicated by the arrows. Inset: A schematic diagram of the multilayer indicating the direction of the *c*-axis [19].

b. The dependence of resistance on temperature for bilayer films consisting of the metal $La_{1.55}Sr_{0.45}CuO_4$, and insulator La_2CuO_4 [21].

Artificially layered superlattices of FeSC could offer a unique opportunity towards tailoring superconducting properties and understanding the mechanisms of superconductivity by creating model structures that do not exist in nature. For high field

applications, very high J_c and H_{irr} are indispensable along all crystal directions. On the other hand, the development of superconducting devices, such as tunnel junctions, requires multilayered heterostructures. For these two different requirements, we conducted research to find two different interlayer materials. The first interlayer material should produce *ab*-aligned nanoparticle arrays by layering and self-assembled *c*-axis aligned defects that combine to produce very large J_c and H_{irr} enhancements over a wide angular range. The other interlayer material should demonstrate a structurally modulated superlattice with atomically sharp interfaces suitable for superconductor/normal metal/superconductor (SNS) or superconductor / insulator / superconductor (SIS) tunnel junctions.

I-5. Effect of strain on the T_c of iron-based superconductor thin films

Enormous strains can exist in thin films when one material is deposited on another due to differences in crystal lattice parameters and thermal expansion behavior between the film and the underlying substrate or arising from defects formed during film deposition. As a result, the properties of thin films can be dramatically different from the intrinsic properties of the corresponding unstrained bulk materials [22-25]. While such strain often leads to degraded film properties, the judicious use of substrates and growth parameters offers the opportunity to enhance particular properties of a chosen material in thin film form, namely strain engineering. In particular, strain in FeSC thin films could affect the T_c of the films. Based on the 1111 phase work, applied physical or chemical pressure in bulk single crystal could increase T_c up to ~56K [4-6]. For the 11 phase, many groups reported thin films with higher T_c than in the bulk phase due to strain [26-28]. For the 122 phase,

Iida et al. reported the dependence of T_c on the strain [29]. They used various substrates to examine the strain in Co-doped Ba-122. According to what we learned from the epitaxial growth of Co-doped Ba-122 on various substrates, Co-doped Ba-122 grown on $SrTiO_3$ substrate demonstrates a better quality than other substrates [30]. Therefore, it is not possible to exclude the extrinsic substrate effect on the quality of thin films. For this thesis, we studied the intrinsic strain effect in Co-doped Ba-122 through the thermal expansion mismatch between Co-doped Ba-122 and the substrate.

References

[1] H. K. Onnes, Leiden Comm., 120b, 122c, 124c (1911).

[2] Y. Kamihara *et al*., *J. Am, Chem. Soc*. **128**, 10012 (2006).

[3] Y. Kamihara *et al*., *J. Am, Chem. Soc*. **130**, 3296 (2008).

[4] H. Takahashi *et al*., *Nature* **453**, 376 (2008).

[5] X. H. Chen *et al*., *Nature* **453**, 761 (2008).

[6] C. Wang *et al*., *Euro Phys. Lett*., **83,** 67006 (2008).

[7] W. Malaeb, Ph. D. thesis at Univ. of Tokyo, (2009).

[8] M. Rotter *et al*., *Phys. Rev. Lett*. **101,** 107006 (2008).

[9] A. S. Sefat *et al*., *Phys. Rev. Lett*. **101,** 117004 (2008).

[10] X. C. Wang *et al*., *Solid State Communications* **148,** 538 (2008).

[11] F.-C. Hsu *et al*., *Proc. Natl. Acad. Sci. USA* **105,** 14262 (2008).

[12] H. Hiramatsu *et al*., *Appl. Phys. Lett*. **93,** 162504 (2008).

[13] S. Haindl *et al*., *Phys. Rev. Lett*. **104,** 077001 (2010).

[14] H. Hiramatsu *et al*., *Applied Physics Express* **1**, 101702 (2008).

[15] T. Katase *et al*., *Solid State Communications* **149,** 2121 (2009).

[16] E. M. Choi *et al*., *Appl. Phys. Lett.* **95**, 062507 (2009).

[17] H. Hilgenkamp *et al*., *Rev. Mod. Phys.* **74**, 485 (2002).

[18] D. Dimos *et al*., *Phys. Rev. Lett*. **61,** 219 (1988).

[19] J. M. Triscone *et al*., *Phys. Rev. Lett*. **64,** 804 (1990).

[20] Y. Suzuki *et al*., *Phys. Rev. Lett*. **73,** 328 (1994).

[21] A. Gozar *et al*., *Nature* **455**, 782 (2008).

[22] R. S. Beach *et al*., *Phys. Rev. Lett*. **70**, 3502 (1993).

[23] I. Bozovic, *et al*., *Phys. Rev. Lett*. **89**, 107001 (2002).

[24] H. Haeni *et al*., *Nature* **430**, 758 (2004).

[25] K. J. Choi *et al*., *Science* **306**, 5698 (2004)

[26] W. Si *et al*., *Appl. Phys. Lett*. **95,** 052504 (2009).

[27] E. Bellingeri *et al*., *Appl. Phys. Lett*. **96,** 102512 (2010).

[28] I. Tsukda, *et al*., *Appl. Phys. Express* **4,** 053101 (2011).

[29] K. Iida *et al*., *Appl. Phys. Lett*. **95,** 192501 (2009).

[30] S. Lee *et al*., *Nature Mater.* **9,** 397 (2010).

Chapter II. Experimental Setup

II-1. Pulsed laser deposition system

Pulsed laser deposition (PLD) is one of the physical vapor deposition methods used to grow epitaxial thin films. The most advantageous reason to grow films with PLD is a stoichiometric flux transfer from multi-components target materials to thin films. Therefore, PLD has been widely used to grow complex oxide systems and high temperature superconductors. It was reported that Co-doped AE-122 (Sr-122 or Ba-122) were grown by PLD in a high vacuum [1-2]. In this study, we grew Co-doped Ba-122 thin films on various substrates and templates by PLD with a Lambda Physik LPX-305i, KrF excimer laser (wavelength: 248nm). Beam size was varied by applying various masks in the range of 1×3 mm^2 ~ 2×4 mm^2. The PLD system was set up with multiple target capabilities using a six target carousel. Target changing and laser triggering were controlled with an automated LabVIEW program.

Figure II.1 and II.2 show the schematic and photos of our PLD system. The plumes generated by laser ablation during the thin film deposition can be seen in Fig. II.2b. The vacuum chamber was set up with a turbo molecular pump and a rotary vane pump to provide low base pressure at 1×10^{-7} Torr. The 2" resistive heater was used to set the substrate temperature up to 800^{o}C during the deposition. The Co-doped Ba-122 targets were prepared by a solid-state reaction with a nominal composition of Ba : Fe : Co : As = 1 : 1.84 : 0.16 : 2.0~2.2.

.

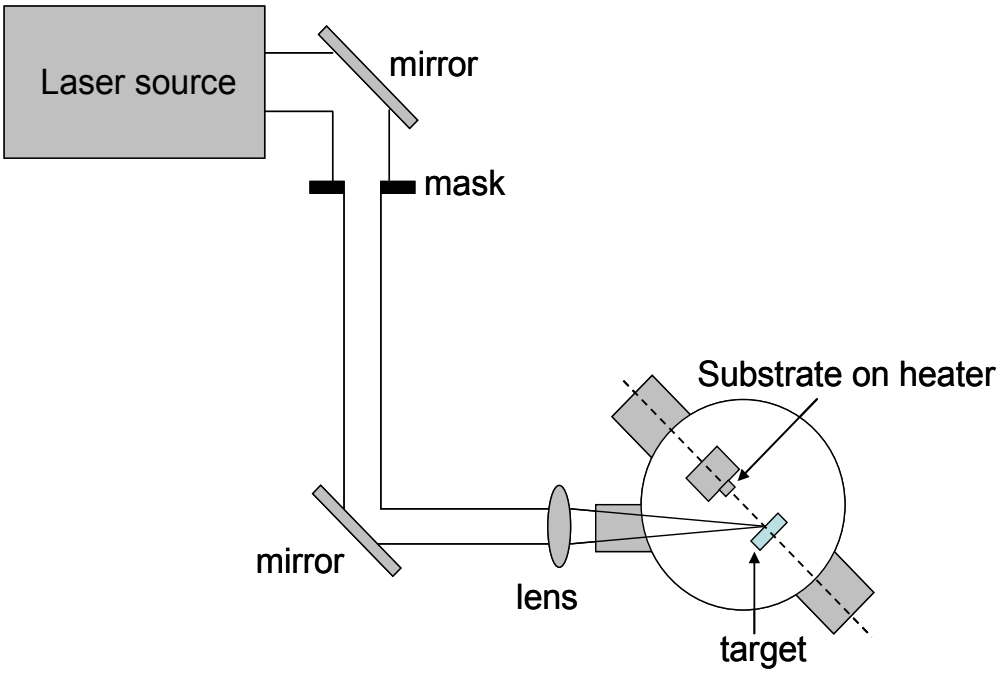

Figure II.1. **Schematic of pulsed laser deposition system.** The laser beam edge was cut by the mask to remove all non-uniform energy areas. The target is located on the focused spot.

a **b**

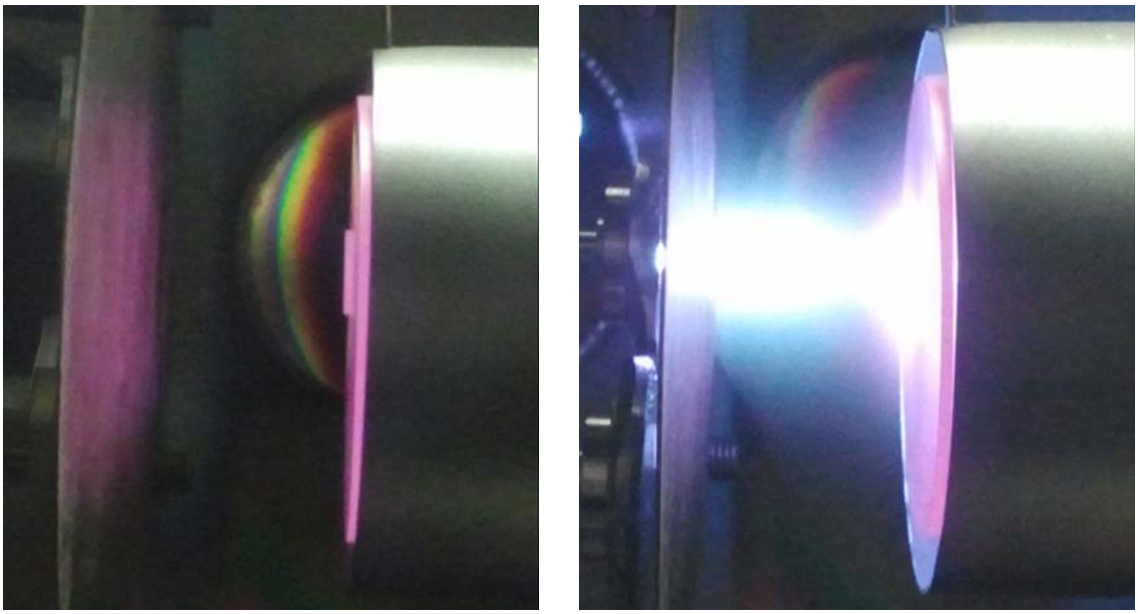

Figure II.2. Pictures of thin film deposition procedure.

a. Substrate heated up to 750 ^{o}C by resistive heater

b. Plume generated by laser ablation during the deposition

II-2. X-ray diffraction measurement

Four-circle x-ray diffraction (XRD) was used to analyze the phase purity, crystal structure, epitaxial arrangements, and periodicity of the thin films and superlattices. A four-circle XRD system can access reciprocal lattices through θ, 2θ, φ, and χ scans, as shown in Fig. II.3.

The crystalline quality of the thin films were determined by the full width at half maximum (FWHM) of the rocking curve x-ray scan. The crystallographic orientation, strain state, and identification of phases were determined with θ-2θ scans. The in-plane texture was determined by the off-axis azimuthal φ scan. Finally, the in-plane mosaic spread was determined by the FWHM of azimuthal φ scan of off-axis reflections.

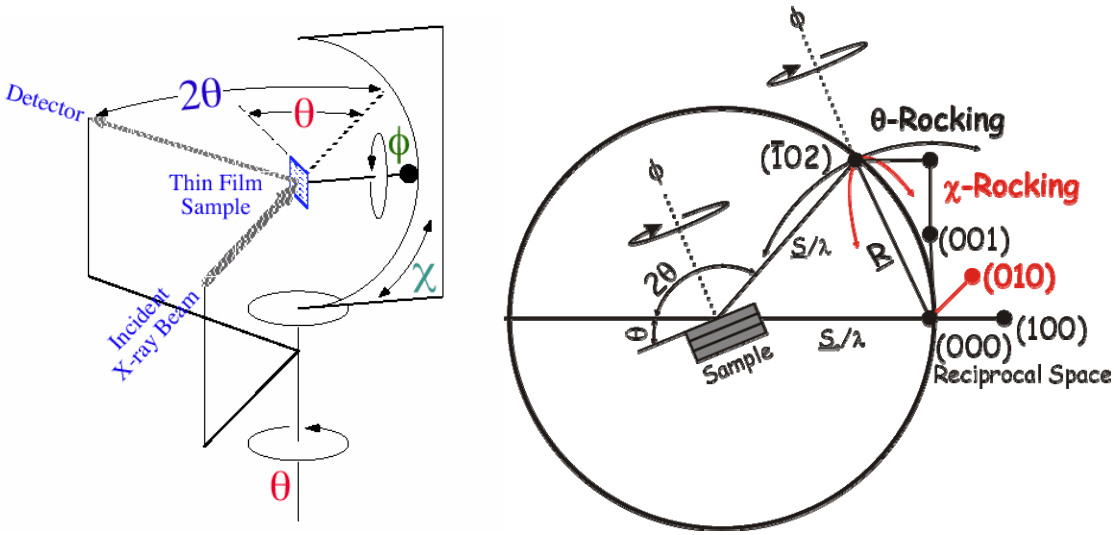

Figure II.3. Illustrations of four circle x-ray in the real space and reciprocal space [3].

II-3. Electrical transport and electromagnetic measurement

Transition temperature and normal state resistivity were measured by the Van der Pauw method in a cryostat cooled by a closed cycle refrigerator. Typical sample size was 10×10 mm^2. Each of the four corners of the samples was connected by wires that were connected to a Keithley 2400 current source and a Keithley 182 digital voltmeter. Electromagnetic properties such as critical current density (J_c), irreversibility field (H_{irr}) and angular dependence of J_c were measured by both transport and magnetization. The magnetization on a 2 mm x 4 mm size sample was measured in a 14 T Oxford vibrating sample magnetometer (VSM) at 4.2K with the applied field perpendicular to the film surface. Magneto-optical imaging was used to examine the uniformity of current flow in the films to validate the use of the Bean model for converting the magnetic moment measured in the VSM to J_c assuming current circulation across the whole sample without granular effects. For a thin film, $J_c = 15\Delta m/(V\ r)$, where Δm is the width of the hysteresis loop in emu, V the film volume in cm^3, and r the radius corresponding to the total area of the sample size, as calculated by πr^2 = a x b (a and b are the film width and length in cm, respectively) [4].

References

[1] H. Hiramatsu *et al*., *Applied Physics Express* **1**, 101702 (2008).

[2] T. Katase *et al*., *Solid State Communications* **149,** 2121 (2009).

[3] D. G. Schlom *et al*., *J Mater Res* **11**, 1336 (1996).

[4] S. Lee *et al*., *Nature Mater.* **9,** 397 (2010).

Chapter III. Template engineering of Co-doped $BaFe_2As_2$ single-crystal thin films

III-1. Scientific issue about the iron based superconductor growth

Epitaxial pnictide thin films have so far been hard to produce, especially the F-doped highest T_c rare earth (RE) 1111 phase [1-2]. Because both As and F are volatile at the deposition temperature, it is difficult to control the overall stoichiometry of the deposited film [1]. By contrast, Co, which can be used as the dopant in $Ba(Fe,Co)_2As_2$ (Ba-122), has a low vapour pressure under growth conditions. Alkaline earth (AE) 122 phases have been grown on (001) oriented $(La,Sr)(Al,Ta)O_3$ (LSAT) and $LaAlO_3$ (LAO) single-crystal substrates by several groups [3-5]. However, the quality of the films reported was not satisfactory because $T_{c,\rho=0}$ and ΔT_c are 14~17K and 2~4K, respectively, values which were much lower and broader than those of bulk single crystals [6]. Furthermore, J_c (5K, SF) of these films was ~10kA/cm^2, one to two orders of magnitude lower than in bulk single crystals [6]. We believe a fundamental reason for the low quality of the AE-122 phase on these substrates is that AE-122 is a metallic system, which does not bond well with oxide single-crystal substrates. In particular, LSAT and LAO substrates contain trivalent cations, whereas the alkaline earths of Ba-122 or Sr-122 are divalent, making the bonding between the substrate and Ba-122 poor, which leads to a non-epitaxial, granular and poorly connected superconducting phase whose grains are separated by high-angle grain boundaries, wetting GB phases such as FeAs, and/or off-stoichiometric grains [7].

III-2. Template engineering using titanates oxide layer

To overcome these problems, we explored the use of a template consisting of thin epitaxial layers of the divalent, AE-containing $SrTiO_3$ (STO) or $BaTiO_3$ (BTO) between various single-crystal perovskite substrates and the Ba-122 film. Building upon this common feature, we established the bonding model described in Fig. III.1.

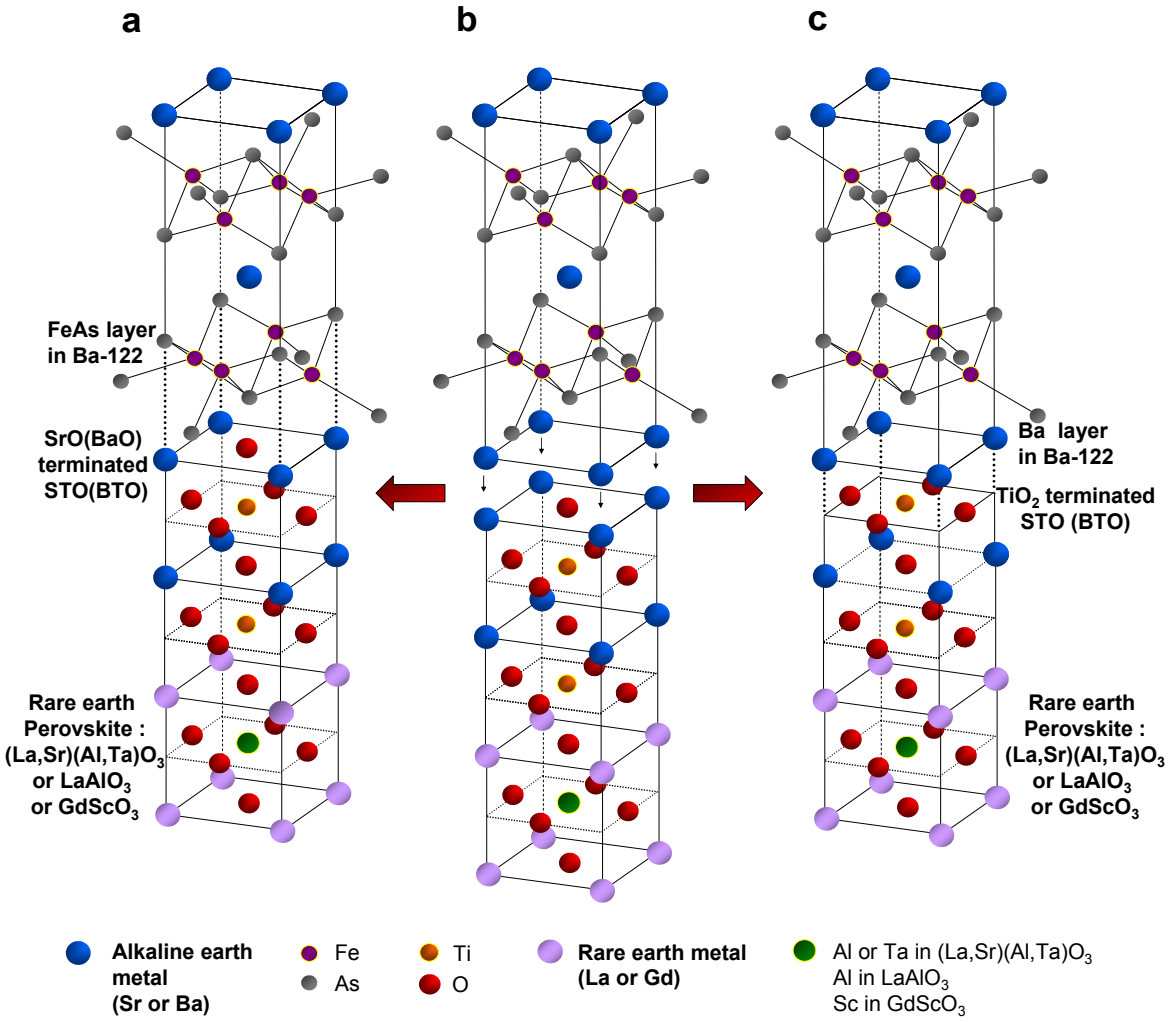

Figure III.1. **Schematic model of Ba-122 deposition on STO(BTO) template grown on various oxide substrates.** b, the Ba-122 unit cell and the alkaline earth titanium oxide (AETO) unit cells grown on rare earth (RE) perovskite oxide substrates unit cell. In this example only two unit cells of AETO and one unit cell of RE-perovskite are shown. There

are two possible ways the Ba-122 and perovskite lattice bonding can occur. a, the FeAs layer in Ba-122 bonds strongly to AE-O terminated RETO as Ba-122 is deposited (the AE-O layer from AETO replaces the Ba layer in Ba-122). c, the Ba layer in Ba-122 bonds strongly to TiO_2 terminated RETO as B-122 is deposited (the Ba layer from Ba-122 replaces AE-O in the AETO).

We grew a proof-of-principle of this concept by growing Co-doped Ba-122 epitaxial thin films on (001) oriented STO substrates with J_c over 1 MA/cm^2 (4.2K, SF), values significantly higher than in previously reported epitaxial thin films. However, the STO substrates became electrically conducting during deposition of the Co-doped Ba-122 thin film at 730 ^{o}C in the high vacuum (2.7×10^{-5} Pa), due to formation of oxygen vacancies in the STO [8]. This provides a parallel, current-sharing path between Ba-122 and STO which compromises normal-state property studies. Clearly normal-state behaviour and potential device applications [9] need insulating substrates, especially microwave devices which need substrates such as LSAT or LAO that have a low dielectric constant.

We successfully grew single-crystal Co-doped Ba-122 epitaxial thin films using thin STO or BTO templates deposited on various perovskite single-crystal substrates, which include (001) LSAT, (001) LAO, and (110) $GdScO_3$, all of which yield Ba-122 films with superior superconducting properties on insulating substrates. The 50-100 unit cell (u.c.) thick STO and BTO templates were grown by pulsed-laser deposition (PLD) using a KrF excimer laser (248 nm) with high oxygen pressure reflection high energy electron diffraction (RHEED) for digital control and *in situ* monitoring of the epitaxial growth. Co-

doped Ba-122 films ~350 nm thick were grown on both bare single-crystal substrates and substrates with STO and BTO templates. Structural and superconducting properties of these films are listed in Table III.1.

Table III.1. Crystalline quality and superconducting properties of the Ba-122 films grown on various bare and on STO- or BTO-templated substrates. As a reference, bulk single-crystal properties are also shown at the bottom. Lattice mismatch with respect to the top most oxide substrate, FWHM of rocking curve of Ba-122 (004) reflection, $\Delta\phi$ of azimuthal ϕ scan, and existence or non-existence of extra peaks due to misoriented grains in the ϕ scan are shown as measures of the out-of-plane and in–plane crystalline quality. $T_{c,\rho=0}$, ΔT_c, and J_c characterize the superconducting properties

Co-doped Ba122 thin films on	Lattice mismatch (%)	FWHM $\Delta\omega$ (°)	FWHM $\Delta\phi$ (°)	Extra peaks in ϕ scan	$T_{c,\rho=0}$ (K)	ΔT_c (K)	J_c (4.2K, SF) (A/cm^2)
Bare STO	**-1.7**	**1.43**	**1.6**	**No**	**19.2**	**0.7**	**1.1X10^6**
Bare LSAT	**-2.6**	**3.10**	**4.4**	**Yes**	**14.3**	**6.8**	**< 1X10^4**
100uc STO/LSAT	**-2.6**	**0.55**	**0.8**	**No**	**21.5**	**1.3**	**2.9X10^6**
50uc BTO/LSAT	**-2.6**	**0.17**	**0.6**	**No**	**20.8**	**1.3**	**4.5X10^6**
Bare LAO	-4.7	2.10	4.1	Yes	15.3	2.5	
50uc STO/LAO	-4.7	0.95	1.2	No	19.8	1.4	
Bare GSO	~0	0.62	0.7	Yes	16.5	4.4	
50uc STO/GSO	~0	0.24	0.3	No	20.9	1.2	
100uc BTO/GSO	~0	0.24	0.5	No	19.0	1.3	
200uc STO/Si	-1.4	0.80	1.0	No	18.0	1.0	1.5X10^6
Bulk single crystal Ba122		0.18			21.4	0.6	0.4 X10^6

We discuss here only films grown on bare STO, bare LSAT, STO/LSAT (i.e. an STO template on LSAT), and BTO/LSAT, while emphasizing that similar properties were obtained on (001) LAO and (110) $GdScO_3$ too (see Table III.1).

III-3. Structural properties of Co-doped Ba-122 thin films

Figure III.2a and its inset show an atomic force microscope (AFM) image of a 100 u.c. STO template on LSAT and its RHEED pattern. They show atomically-flat terraces and single unit-cell high (~4 Å) steps, which confirm that the STO template layer is as good as those of bulk single crystal substrates of STO. It is found that an STO template up to 100 u.c. is fully coherent with the LSAT substrate. The epitaxial and crystalline quality of the Co-doped Ba-122 thin films were measured by four-circle x-ray diffraction (XRD). Figure III.2b shows the out-of-plane θ-2θ scans of the films on bare LSAT and 100 u.c. STO/LSAT. The XRD patterns show that the film 00*l* reflections dominate, which indicates *c*-axis growth normal to the template and substrate. An extra peak at 2θ = ~65^o in the film grown on STO/LSAT is the 002 reflection from Fe [4], however with intensity less than 0.5% of the Ba-122 (004) reflection. The intensity of the Ba-122 00*l* peaks on STO/LSAT is about 2 orders of magnitude higher than that on bare LSAT. This indicates that the film on STO/LSAT is highly *c*-axis oriented while the film on bare LSAT is weakly *c*-axis textured polycrystalline normal to the substrates. Rocking curves for the 004 reflection were measured to determine the out-of-plane mosaic spread and crystalline quality. As shown in Fig. III.2c, the full width at half maximum (FWHM) of the 004 reflection rocking curve of the film on STO/LSAT is as narrow as 0.55^o, whereas that of the film on bare

LSAT is as broad as 3.1°. Remarkably, the FWHM of the film on BTO/LSAT is as narrow as 0.17° similar to that of a Ba-122 bulk single crystal [10] (see Table III.1).

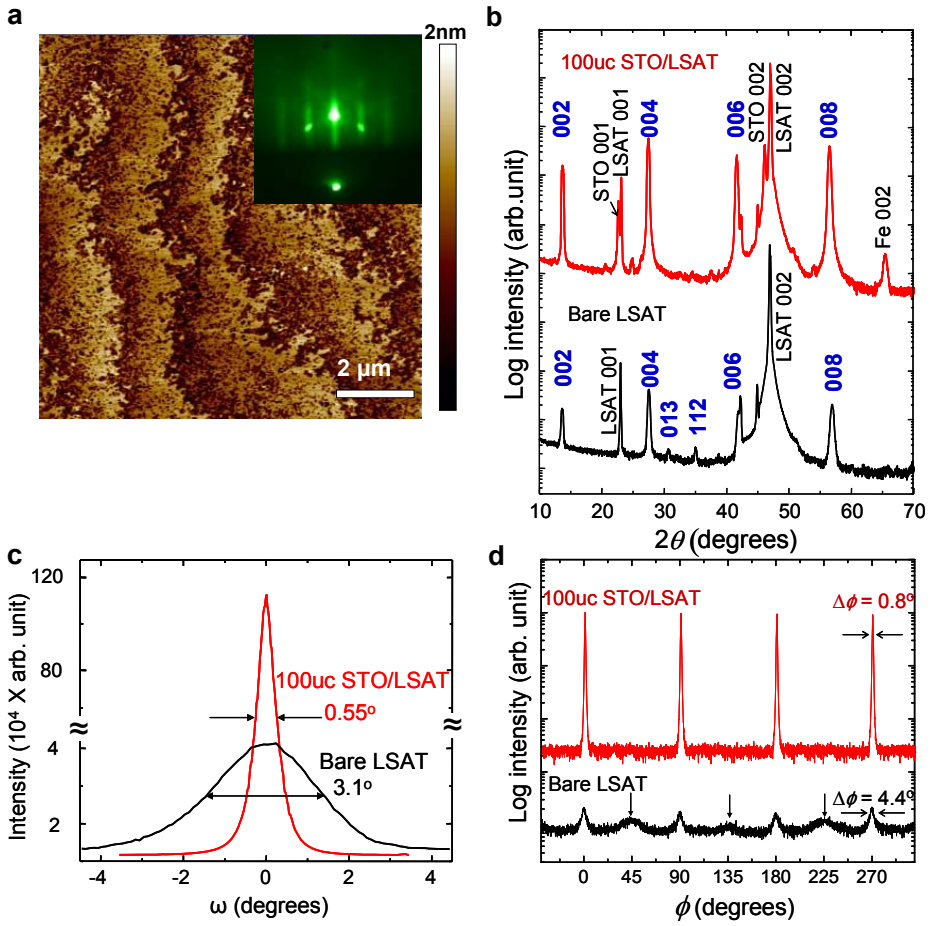

Figure III.2. AFM image and RHEED pattern of the STO template grown on LSAT, and XRD patterns obtained on the Co-doped $BaFe_2As_2$ thin films. a, AFM image of 100 u.c. STO template grown on LSAT. The RHEED pattern of Ba-122 is shown in the inset. b, Out-of plane θ-2θ XRD patterns of the film grown on 100 u.c. STO/LSAT and the film grown on bare LSAT. All non-identified small peaks are reflections of identified peaks due to CuKβ and CuKα+β. c, Rocking curve and FWHM for (004) reflection of Ba-122. d,

Azimuthal ϕ scan and $\Delta\phi$ of the off-axis 112 reflection of Ba-122. The vertical arrows above the bare LSAT pattern indicate a peak due to misoriented grains separated by high-angle grain boundaries.

In-plane texture and epitaxial quality were determined by azimuthal ϕ scans of the off-axis (112) peak, as shown in Figure III.2d. The film grown on bare LSAT shows broad major peaks ($\Delta\phi$=4.4^o) every 90^o with additional broader intermediate-angle peaks, which indicates that the in-plane Ba-122 structure consists of grains with high-angle tilt grain boundaries (GB). In contrast, the film grown on 100 u.c. STO/LSAT shows only sharp, strong peaks ($\Delta\phi$=0.8^o) every 90^o characteristic of a truly epitaxial film with perfect in-plane texture. Our Ba-122 thin films are fully strain relaxed. The in-plane and out-of-plane lattice parameters of all of our Ba-122 films are the same as the bulk single crystal values.

To verify the crystalline quality, microstructures were studied by transmission electron microscopy (TEM). Figures III.3a-d show the cross-sectional TEM images of the films grown on bare LSAT (Fig. III.3a), 100 u.c. STO/LSAT (Fig. III.3b), 20 u.c. STO/LSAT (Fig. III.3c), and bare STO (Fig. III.3d). The inset in the top right corner of Fig. III.3a, 3b, and 3d shows the corresponding Ba-122 selected area electron diffraction (SAED) patterns, respectively. The Ba-122 films on bare STO and on STO templated LSAT show epitaxial relationships between the films and the substrate, while the film on bare LSAT shows a granular microstructure with many misoriented grains. The inset on the left side of Fig. 3a shows the HRTEM image of a high angle grain boundary. The high

resolution TEM image in Fig. III.3c shows the structure of interfaces between STO and LSAT and between STO and Ba-122.

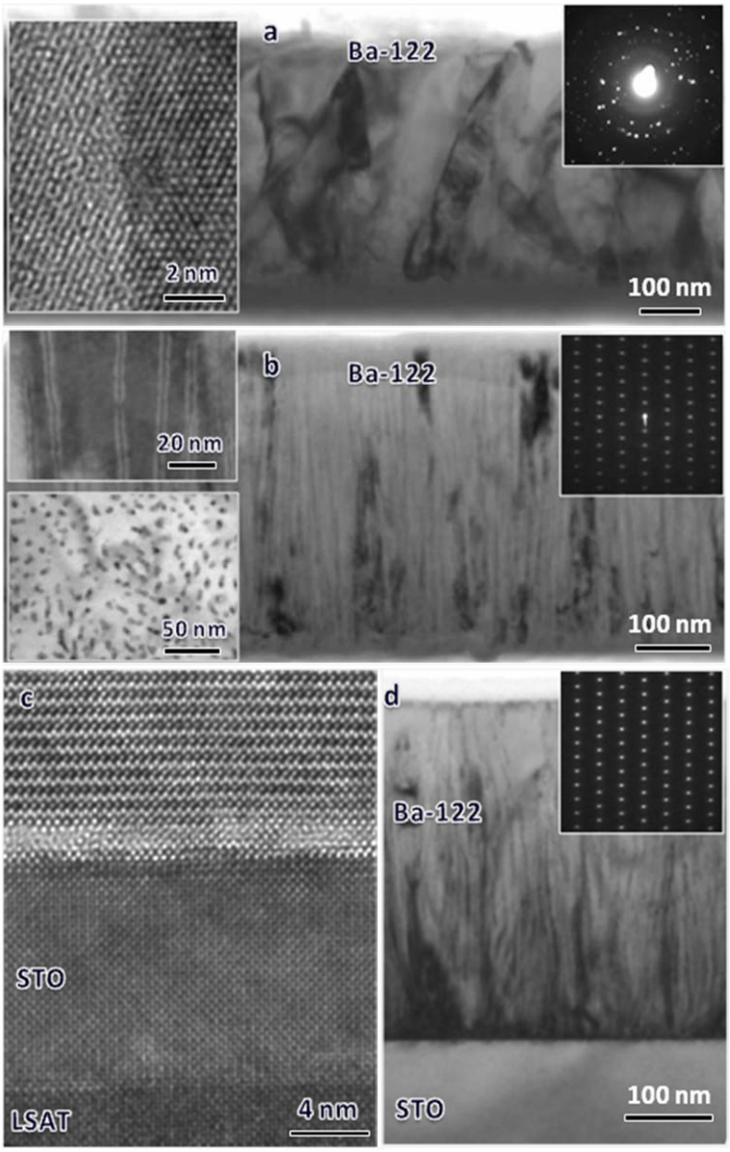

Figure III.3. Cross-sectional TEM micrographs of films on a, bare LSAT, b, 100 u.c. STO/LSAT, c, 20 u.c. STO/LSAT, and d, bare STO. They confirm that the films on bare STO or STO buffered LSAT are epitaxial, while the film on bare LSAT is polycrystalline with misoriented grains. Line defects along the *c*-axis exist in the films grown on

STO/LSAT and bare STO. The insets on the left side of b are planar and cross-sectional view of the same film, showing a uniform distribution of the vertically aligned line defects. The inset on the top right side of a, b, and d shows the corresponding SAED patterns. The HRTEM image in c shows the interface structures between LSAT and 20 u.c. STO and between 20 u.c. STO and the Ba 122 film.

The localized disorder of atomic arrangement at the STO/Ba-122 interface may be due either to interface reaction or to the ion beam damage during TEM sample preparation. The epitaxial films grown on bare STO and on STO/LSAT show vertically aligned line defects seen in the cross-sectional TEM images of Figs. III.3b and 3d as well as in the top-left side inset in Fig. III.3b. The inset in the bottom-left corner of Fig. III.3b shows a planar view TEM image of the same film, revealing that the vertically aligned defects are uniformly distributed. Both x-ray energy dispersion spectroscopy and electron energy-loss spectroscopy reveal that the line defects consist of secondary phase consisting mainly of Ba and O and depleted of Fe, Co and As.

III-4. Superconducting properties of Co-doped Ba-122 thin films

To characterize the superconducting transition temperature T_c, resistivity was measured as a function of temperature (ρ-T) by the van der Pauw method. As shown in Fig. III.4a, the residual resistivity ratio (RRR) of the Ba-122 film grown on bare STO is as high as 160, a value consistent with oxygen deficient STO [8] that we reproduced on bare STO substrates heated in vacuum under the same conditions used for Ba-122 deposition.

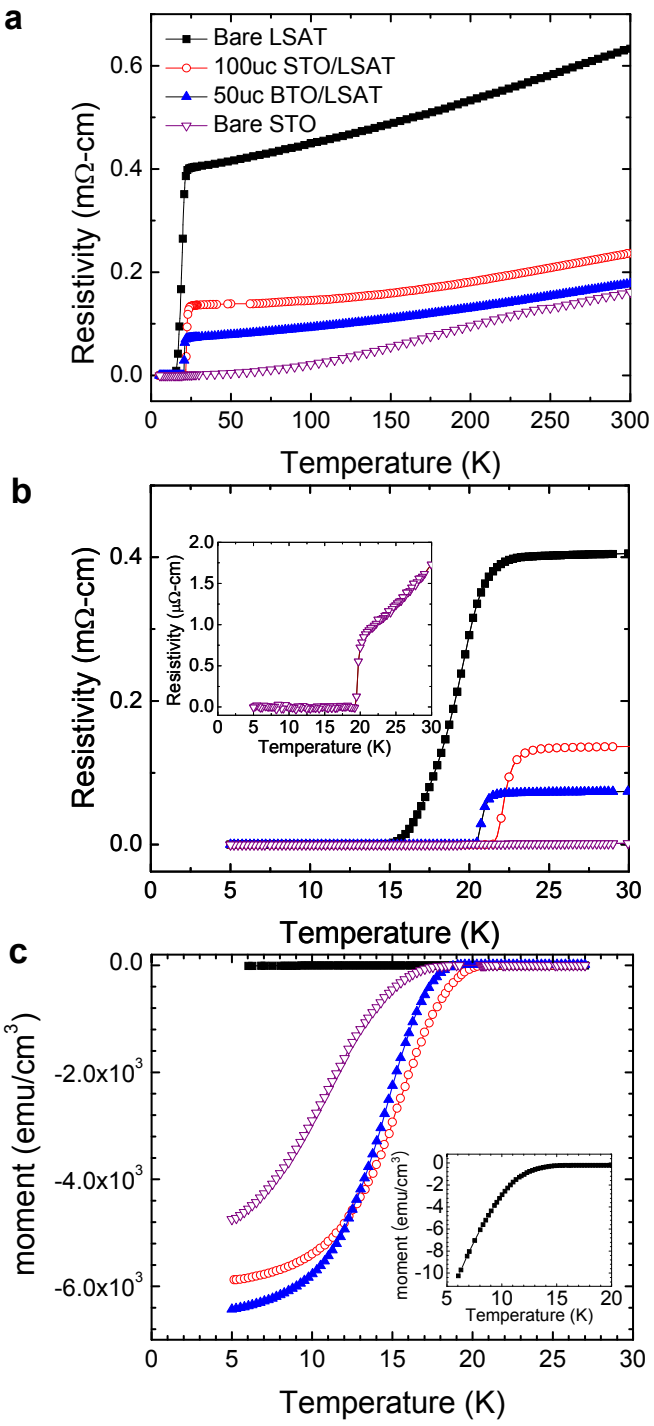

Figure III.4. Resistivity and magnetic moment as a function of temperature. a, $\rho(T)$ from room temperature to below T_c. b, Superconducting transition of all films; $T_{c,\,onset}$ and $T_{c,\,\rho=0}$ of the film on 100 u.c. STO/LSAT are as high as 22.8K and 21.5K, respectively.

Inset shows superconducting transition of the film on bare STO. c, Magnetic moment as a function of temperature evaluated by warming after zero-field-cooling. A field of 2 mT was applied perpendicular to the plane of the films after cooling to 4.2K. Inset shows an expanded view of the much smaller diamagnetic signal of the film grown on bare LSAT.

In contrast, the RRR of films grown on STO/LSAT and BTO/LSAT templates were 1.8 and 2.4, respectively, values characteristic of Co-doped Ba-122 single-crystals [10]. Additionally we noted that the room temperature resistivity of a film on bare LSAT is much higher than a film grown on templated LSAT, which we interpret as being due to strong scattering at the high-angle GBs.

As shown in Fig. III.4b, all films show high $T_{c,\,\rho=0}$ and narrow ΔT_c except for the film with high-angle GBs grown on bare LSAT. In particular, $T_{c,\rho=0}$ of the film on 100 u.c. STO/LSAT is as high as 21.5K and ΔT_c is as narrow as 1.3K, which are the highest and narrowest values ever reported for AE-122 thin films.

Fig. III.4c shows the zero-field-cooled magnetization T_c transitions. All three epitaxial films have a strong diamagnetic signal, in contrast to the polycrystalline film grown on bare LSAT, which, as shown by the inset in Fig. III.4c, shows a three orders of magnitude smaller diamagnetic signal than the epitaxial films. This is a clear indication of magnetic granularity associated with the inability of screening currents to develop across the high-angle grain boundaries in the film on bare LSAT.

Fig. III.5a shows J_c as a function of magnetic field for all films determined from vibrating sample magnetometer measurements in fields up to 14 T. Here too all films

except that on bare LSAT show high J_c, over 1 MA/cm^2 (4.2K, SF), which are the highest values ever reported for AE-122 thin films and are even better than in bulk single crystals (0.4 MA/cm^2 at 4.2K) [6]. Remarkably, the J_c of the film on BTO/LSAT is as high as ~4.5 MA/cm^2. Furthermore the J_c of the two epitaxial films on the templates only have a weak field dependence, indicative of little or no suppression of the J_c by strong fields as indicated by the STO/LSAT film which had J_c = ~0.4 MA/cm^2 even at 14 T. The magneto-optical (MO) image of the film on STO/LSAT (inset in Fig. III.5a) shows strong flux shielding and a J_c of ~3 MA/cm^2 (6.6K, 20 mT), similar to that deduced from the magnetization measurements. Such MO images confirm that the epitaxial films grown on STO/LSAT or BTO/LSAT are uniform and well-connected without any weak links.

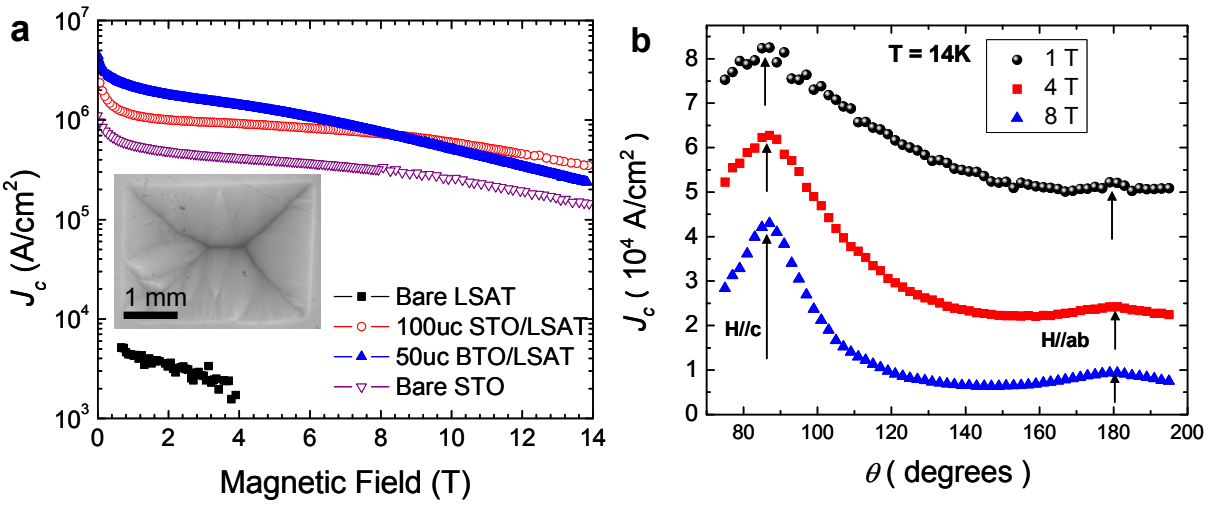

Figure III.5. J_c as a function of magnetic field and its angular dependence. a, Magnetization J_c as a function of magnetic field at 4.2K with the field applied perpendicular to the plane of the film. Inset shows a magneto-optical image obtained by zero-field-cooling to 6.6K, then applying a magnetic 20 mT field perpendicular to the plane

of the film. b, Transport J_c at 14K and 1, 4, and 8T as a function of the angle between the applied field and the surface of the Ba-122 films.

We believe that two factors contribute to the high J_c. First, the films on templated LSAT and bare STO have high epitaxial quality with no high-angle tilt GBs, as confirmed by both XRD and TEM analysis. According to our systematic investigation (The detail about the investigation are discussed in chapter IV), [001] tilt grain boundaries of Ba-122 with θ = 6-24° show significant suppression of supercurrent, making it entirely understandable that randomly oriented high-angle tilt GBs would effectively block supercurrent, as suggested by several recent pnictide film reports [2-5]. Indeed the films grown on bare LSAT developed many high-angle GBs, had almost no flux shielding even in low fields (2 mT) and very low J_c. By contrast, films on templated LSAT and bare STO showed high J_c without evidence of weak links. Interestingly the J_c of the film on STO/LSAT is higher than that of the film on bare STO, which is consistent with our observation of a higher density of line defects in Ba-122 on STO/LSAT than for the film grown on bare STO.

We also measured the angular dependent transport J_c of a STO/LSAT film, as shown in Fig. III.5b. J_c always show a strong *c*-axis peak, which opposes the expected electronic anisotropy since the upper critical field H_{c2} is lower for *H* parallel to *c*-axis, making it clear that there is strong pinning along the Ba-122 *c*-axis that is parallel to the vertically aligned second phase defects. Recently, Maiorov et al. reported a similar angular

dependence in much lower J_c, but granular, Co-doped Sr122 films that they associated with contributions from dilute magnetic pinning [11]

We have also grown Co-doped Ba-122 films on other bare substrates, including (001) LAO and (110) $GdScO_3$ (GSO). In spite of the almost perfect lattice match between Ba-122 and (110) oriented GSO, the film on bare GSO shows poor quality, just like the films grown on bare LAO (see Table III.1). Both bare GSO and LAO films show broad peaks from misoriented grains in the ϕ scan. However, when an intermediate layer of STO or BTO was used as a template on the LAO or GSO, the properties of the Ba-122 films were dramatically enhanced and misoriented grains were not seen. Remarkably, we could also grow a superior quality Ba-122 film on STO/GSO using template engineering with intermediate STO layers which produced a perfect lattice match with Ba-122. The FWHM of the (004) reflection rocking curve and $\Delta\phi$ of Ba-122 on 50 u.c. STO/GSO were very narrow, 0.24^o and 0.3^o, respectively (See Table III.1), values close to those of bulk single crystals [10]. All the above results show that an STO or BTO template is the key to growing high-quality epitaxial Ba-122 films.

III-5. Summary of the chapter

In summary, we have developed a novel template engineering technique to turn granular, low-J_c superconducting films into single-crystal, high-J_c, and truly epitaxial films of Ba-122. J_c in our high-quality epitaxial films is about 10 times greater than in bulk single crystals [6] and ~400 times greater than in previously reported AE-122 films [3-5]. Template engineering results in truly single crystal quality (Table III.1) without any loss of

connectivity due to high angle grain boundaries, while a high density of vertically aligned, second phase line defects results in strong c-axis pinning. We believe that this template technique can be applied not only to perovskite single-crystal substrates, but also to other types of oxide substrates or even semiconductor substrates. Indeed, we have demonstrated this approach yields high-quality Co-doped Ba-122 films on epitaxial STO-template grown on (001) Si substrates [12-13] with $T_{c,\,\rho=0}$ = 18 K, ΔT_c = 1K, and no misoriented grains. (Figs. III.6 and III.7) This approach thus greatly expands substrate choices for high-quality Ba-122 thin films, thus allowing much broader fundamental property investigations of the newly discovered ferropnictide superconductors and parent compounds, as well as for exploring their applications. Furthermore, we expect that epitaxial thin films of other layered intermetallics could be successfully grown on various types of oxide substrates by employing similar template engineering principles.

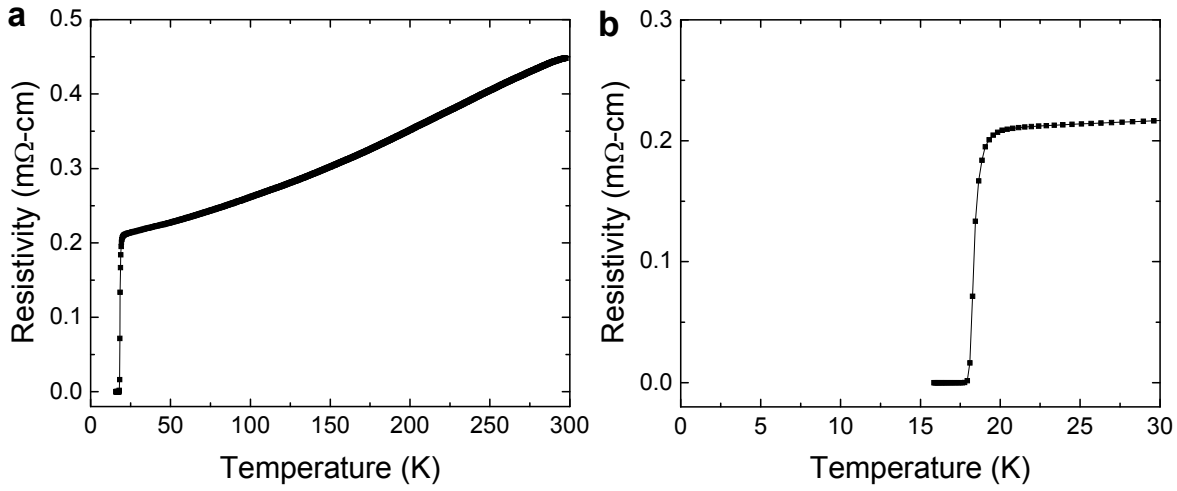

Figure III.6. Resistivity as a function of temperature of Co-doped Ba-122 thin film grown on STO templated Si. a, $\rho(T)$ from room temperature to below T_c. b, Superconducting transition of the film.

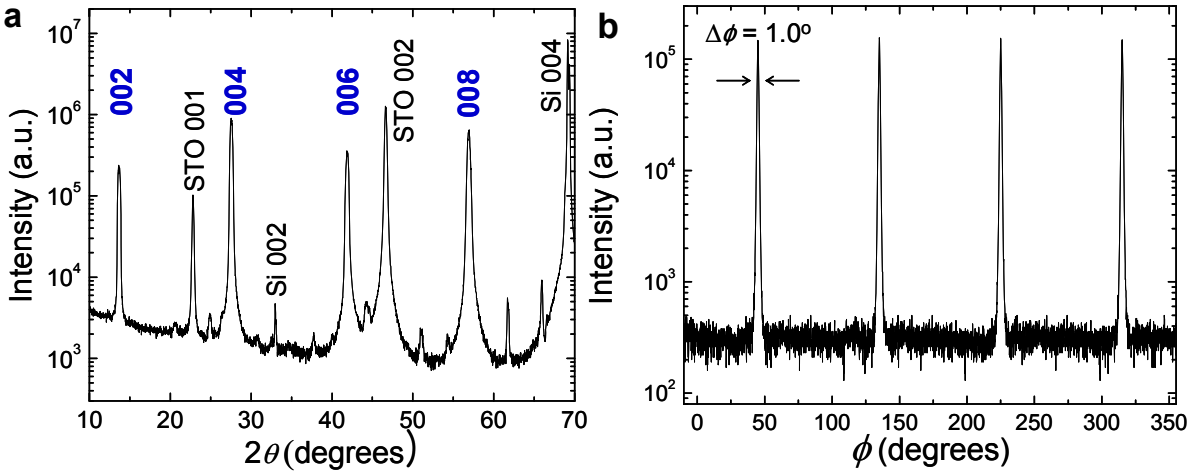

Figure III.7. XRD patterns obtained on the Co-doped $BaFe_2As_2$ thin films grown on STO templated Si. a, Out-of-plane θ-2θ XRD patterns of the film grown on 200 u.c. STO/Si. All non-identified small peaks are reflections of identified peaks due to CuKβ and CuKα+β. b, Azimuthal ϕ scan and $\Delta\phi$ of the off-axis 112 reflection of Ba-122.

References

[1] H. Hiramatsu *et al*., *Appl. Phys. Lett*. **93,** 162504 (2008).

[2] S. Haindl *et al*., *Phys. Rev. Lett*. **104,** 077001 (2010).

[3] H. Hiramatsu *et al*., *Applied Physics Express* **1**, 101702 (2008).

[4] T. Katase *et al*., *Solid State Communications* **149**, 2121 (2009).

[5] E. M. Choi *et al*., *Appl. Phys. Lett.* **95**, 062507 (2009).

[6] A. Yamamoto *et al.*, *Appl. Phys. Lett.* **94,** 062511 (2009).

[7] F. Kametani *et al.*, *Appl. Phys. Lett.* **95,** 142502 (2009).

[8] G. Herranz *et al*., *Phys. Rev. Lett.* **98,** 216803 (2007).

[9] X. Zhang *et al*., *Appl. Phys. Lett.* **95**, 062510 (2009).

[10] X. F. Wang *et al*., *Phys. Rev. Lett.* **102,** 117005 (2009).

[11] B. Maiorov *et al*., *Supercond. Sci. Technol.* **22**, 1 (2009).

[12] R. A. McKee *et al*., *Phys. Rev. Lett.* **81**, 3014 (1998).

[13] L. V. Goncharova *et al*., *J. Appl. Phys.* **100**, 014912 (2006).

Chapter IV. Weak link behavior of grain boundaries in Co-doped $BaFe_2As_2$

IV-1. Scientific issue about grain boundaries in superconductors

In spite of many applications of low-T_c superconductors in magnetic resonance imaging, magnets, particle accelerators and fusion reactors, higher temperature superconductors (HTS) would greatly benefit all applications in permitting higher operating temperatures or higher magnetic fields. However, only two cuprates have so far found significant conductor use: the low-anisotropy $YBa_2Cu_3O_{7-\delta}$ (YBCO) ($\gamma \sim 5$, $T_c = 90$ K) which has the highest irreversibility field $H_{irr}(T)$ above which a finite J_c is possible, and $(Bi,Pb)_2Sr_2Ca_2Cu_3O_x$ (Bi2223) ($\gamma \sim 30$, $T_c = 110$ K) in which only a weak uniaxial grain texture can be developed. It is the strong current-blocking effect of cuprate GBs with misorientation angles $\theta > 3\text{-}5^o$ [1], which has so seriously delayed high-T_c applications [2,3]. Only recently have coated conductor fabrication processes that eliminate high-angle GBs by producing biaxially textured YBCO conductors which essentially fulfill the reality of the idea of "single crystals by the mile" been developed [4,5]. Despite this immense achievement, what is really needed is a high-T_c round wire, in which GBs transmit current irrespective of their grain misorientation, so that multi-filamentary conductors with high current-carrying capability and low hysteretic AC losses can be produced [2, 6,7]. GBs transparent to current are intrinsic to Nb-Ti (T_c~9K), Nb_3Sn (T_c~18K) and MgB_2 (T_c~39K) [2,6-8]. The Fe based superconductors, which now encompass 4 families of materials, have important application properties, namely T_c up to 55K, H_{c2} of 100 T or more, strong vortex pinning, moderate anisotropy $\gamma = 1$ -8, and H_{irr} close to H_{c2} [9-13], leaving open only the

key question whether GBs can transmit current. Here we report the first explicit study of this vital property, using extensive transport, magneto-optical (MO), low-temperature laser scanning microscopy (LTLSM), and high resolution transmission electron microcopy (HRTEM) investigations of $Ba(Fe_{1-x}Co_x)_2As_2$ (Ba-122) epitaxial thin film bicrystals. Our results unambiguously show a strong intrinsic current-blocking effect of GBs across which the critical current density $J_b(\theta)$ rapidly decreases as the misorientation angle θ between neighboring grains increases.

IV-2. Epitaxial growth of Co-doped Ba-122 on STO bicrystal

The bicrystals of Co-doped Ba-122 were fabricated by epitaxial growth of thin films on (001) $SrTiO_3$ bicrystals with nominally symmetric [100] tilt boundaries with 3^o, 6^o, 9^o, and 24^o misorientation angles. The films were deposited at 730 ^{o}C in vacuum by using pulsed laser deposition with a 248 nm KrF UV excimer laser. The base pressure before deposition was 2 x 10^{-7} Torr. The pressure during the deposition was ~ 2 x 10^{-6} Torr. Epitaxial pnictide films were hard to produce, especially the F and O doped highest T_c RE1111 phase [14], while understanding GB properties in polycrystals has been severely compromised by their multi-phase nature and complex microstructure. Yamamoto *et al.* did deduce significant intergranular transport across randomly misoriented grains of RE1111 bulks, but almost all GBs were coated with a metallic FeAs phase, which masks the intrinsic GB properties [15]. Hiramatsu *et al.* reported epitaxial Co-doped Sr122 thin films grown on (001) (La,Sr)(Al,Ta)O_3 (LSAT) substrates [16] but no J_c measurements. Our Co-doped Ba-122 epitaxial thin films exhibit very high J_c (> 3x10^6 A/cm^2 at 4.2K) and typical

T_c, onset of bicrystal films is ~20K and ΔT_c is as narrow as ~1K. We believe that these films show the best quality among Co-doped Ba-122 films ever reported in early stage.

IV-3. Structural properties of Co-doped Ba-122 grown on STO bicrystal

The epitaxial arrangement, crystalline quality and misorientation angles of the Co-doped $BaFe_2As_2$ bicrystals thin films were characterized by four-circle x-ray diffraction. Out-of plane θ-2θ and in-plane ϕ scans were measured to evaluate the epitaxial quality of the films. Figure IV.1 shows the out-of plane θ-2θ x-ray diffraction scan of a Co-doped $BaFe_2As_2$ film grown on 3^o tilted (001) STO bicrystal substrate.

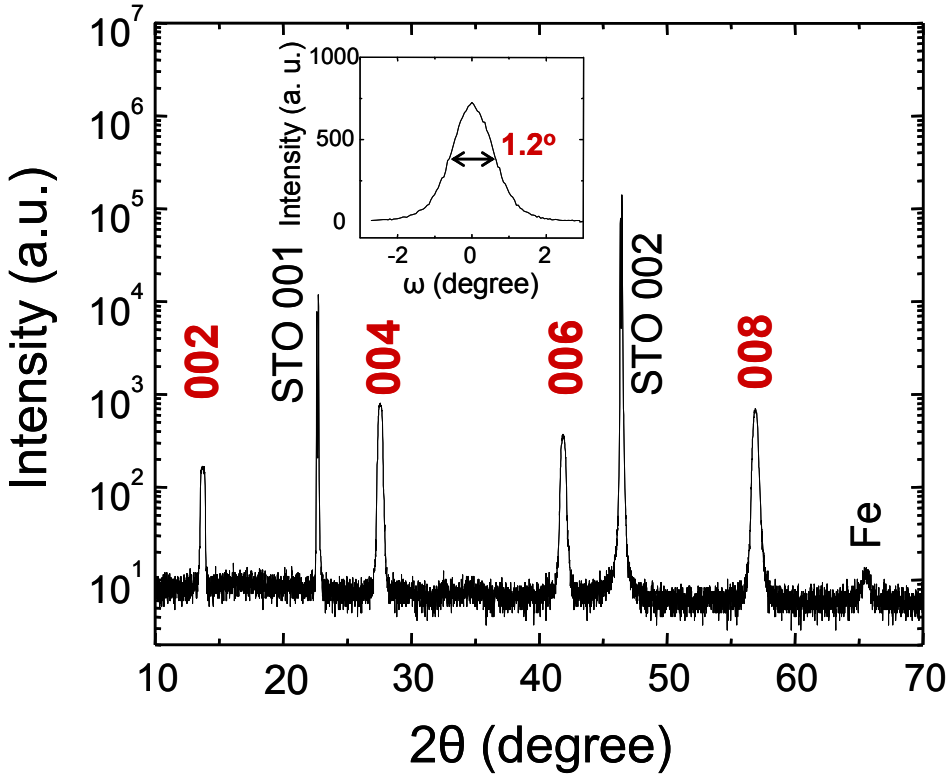

Figure IV.1. XRD θ-2θ scan for a Co-doped $BaFe_2As_2$ film grown on 3^o tilted (001) STO bicrystal substrate. Inset shows the rocking curve scan for 004 reflection.

00*l* peaks are clearly shown which indicate that this film is grown with *c*-axis orientation normal to the substrate. Full width at half maximum (FWHM) of 004 rocking curve (inset of Figure IV.1) is as narrow as 1.2°. Figure IV.2 shows azimuthal off-axis ϕ scan of a Co-doped Ba-122 film grown on 24° tilted (001) STO bicrystal substrate, which shows that the misorientation angles in the Ba-122 film is identical to the $SrTiO_3$ bicrystal substrates without any other misoriented grains.

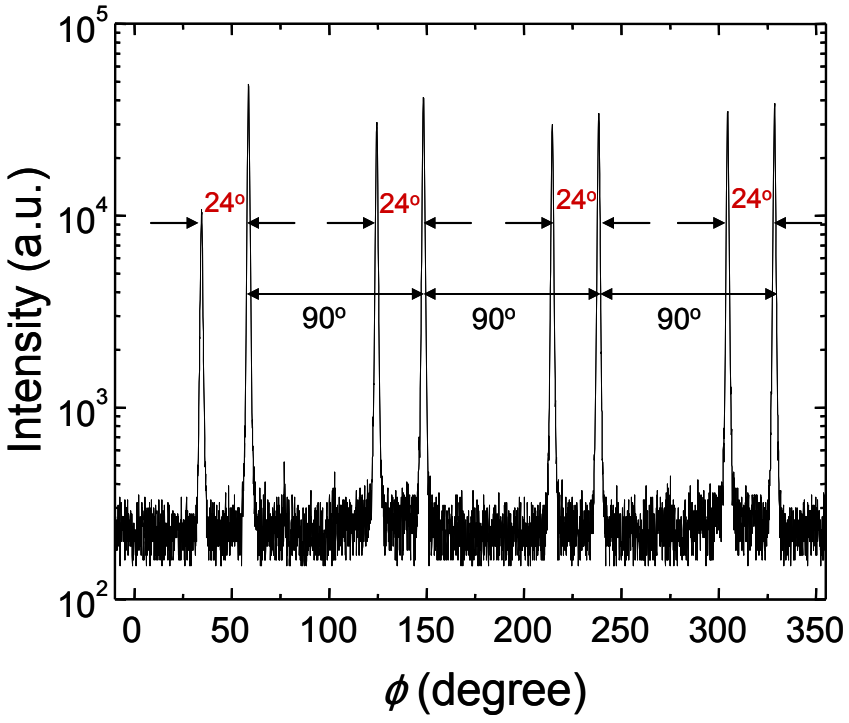

Figure IV.2. Off-axis Azimuthal ϕ scan for a Co-doped $BaFe_2As_2$ film grown on 24° tilted (001) STO bicrystal substrate showing the real misorientation angle of the film bicrystal.

Figure IV.3 shows both a low and a high magnification TEM images of a 24^{o} bicrystal. Transmission electron microscopy (TEM) was performed using JEOL 3011 and JEOL 2010F microscopes. Cross section samples were prepared by mechanical polishing followed by low angle argon ion milling. Cross sectional TEM images of the Ba-122 film show epitaxy which is consistent with XRD results (Figure IV.1). The view direction does not correspond to a zone axis in either side of the film or substrate so the dominate feature is the rows corresponding to the (001) planes. There are no apparent dislocations, faults, or secondary phases at the grain boundary. Chemical composition analysis at the grain boundary by energy dispersive X-Ray spectroscopy (EDS) did not indicate any difference in composition relative to the bulk of the film. The film is quite uniform in thickness over a large area, while the high resolution image shows the (001) planes to be well aligned across the GB and the GB to be without coating secondary phases. We conclude that these are indeed high quality films that yield intrinsic properties.

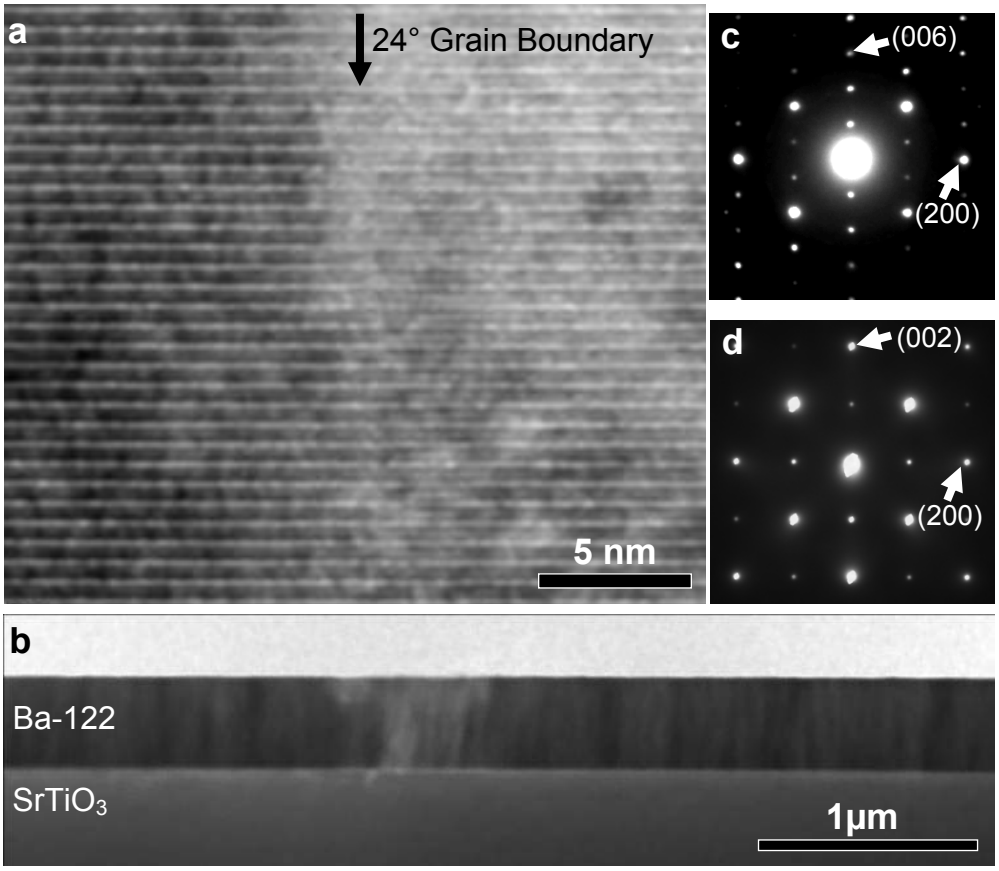

Figure IV.3. TEM micrograph of a cross section of the GB region in a 24° [001] tilt Ba-122 film which confirms that the grains are epitaxial and *c*-axis oriented. The HRTEM image of the grain boundary is shown in (a) viewed parallel to the grain boundary in longitudinal section parallel to the (001) planes. This does not correspond to a zone axis, thus horizontal rows corresponding to the (001) planes rather than atomic columns appear. The (001) planes are well aligned across the grain boundary without observable secondary phases. A lower magnification image from a region with a single grain orientation (b) shows that the film is of uniform thickness. The selected area diffraction pattern of the Ba-122 film along the [010] zone axis is shown in (c) together with the corresponding SAD

pattern for the $SrTiO_3$ substrate (d). The SAD patterns show that the Ba-122 film is single-crystal and *c*-oriented and epitaxially related to the substrate.

IV-4. Evidences of weak link behavior in Co-doped Ba-122

Figure IV.4 shows intergranular resistance curves *R(H,T)* across a 6° [001] tilt GB in high magnetic fields up to 35 Tesla. The resistive transitions are sharp, confirming the high quality of our bicrystal films. Moreover, the lack of broadening of the narrow *R(T)* curves under strong field indicates a typical low-T_c depinning resistive transition with insignificant vortex fluctuations, unlike the strong thermally-activated vortex dynamics and giant flux creep that leads to a big difference between H_{irr} and H_{c2} in the cuprates [17]. By contrast, Figure IV.4 shows that $H_{irr}(T)$ defined by $R(T,H_{irr}) = 0.1\ R_n(T_c)$ is close to H_{c2} defined by $R(T,H_{c2}) = 0.9R_n(T_c)$, as in previous studies of 122 single crystals [11-13]. Here R_n is the normal state resistance. $H_{c2}(T)$ and $H_{irr}(T)$ are very similar for both grain and GB links.

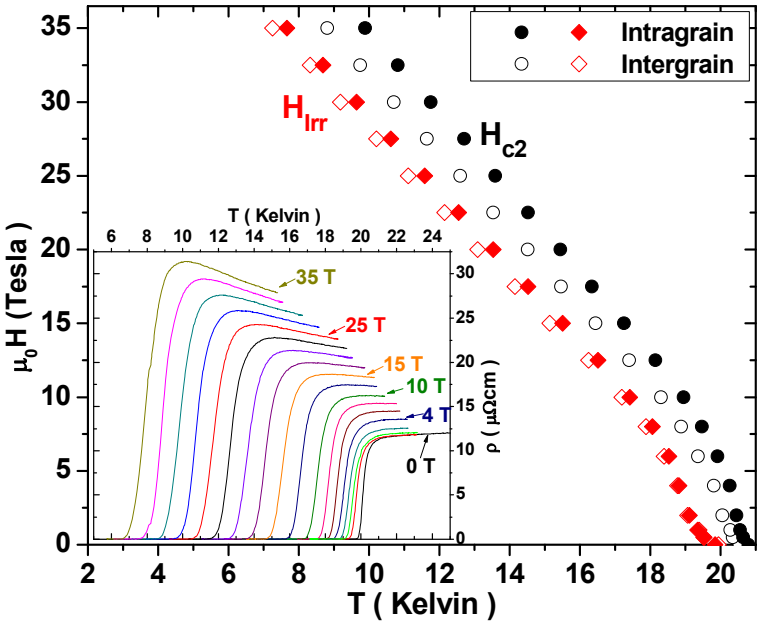

Figure IV.4. Irreversibility field H_{irr} and upper critical field H_{c2} defined by the 10% and 90% points of the normal state resistance $R_n(T_c)$ on resistive transition curves $R(T,H)$ across a 6° [001] tilt GB and its neighboring grain with field applied perpendicular to the film. Inset: resistive transitions up to 35 T across the grain boundary.

Shown in Figure IV.5 are representative LTLSM and MO images of 6° and 9° bicrystals, which demonstrate the significant current-blocking effect of even low-angle GBs. For instance, the LTLSM image in Figure IV.5a of the electric field **E** of the transport current flowing through GB shows a 23 times enhancement at the 6° [001] tilt GB. The MO image in Figure IV.5b shows that the 9° [001] tilt GB is also a strong obstacle for the magnetization currents which make a nearly 90° turn at the GB because it can transmit only about 10% of the intragrain critical current.

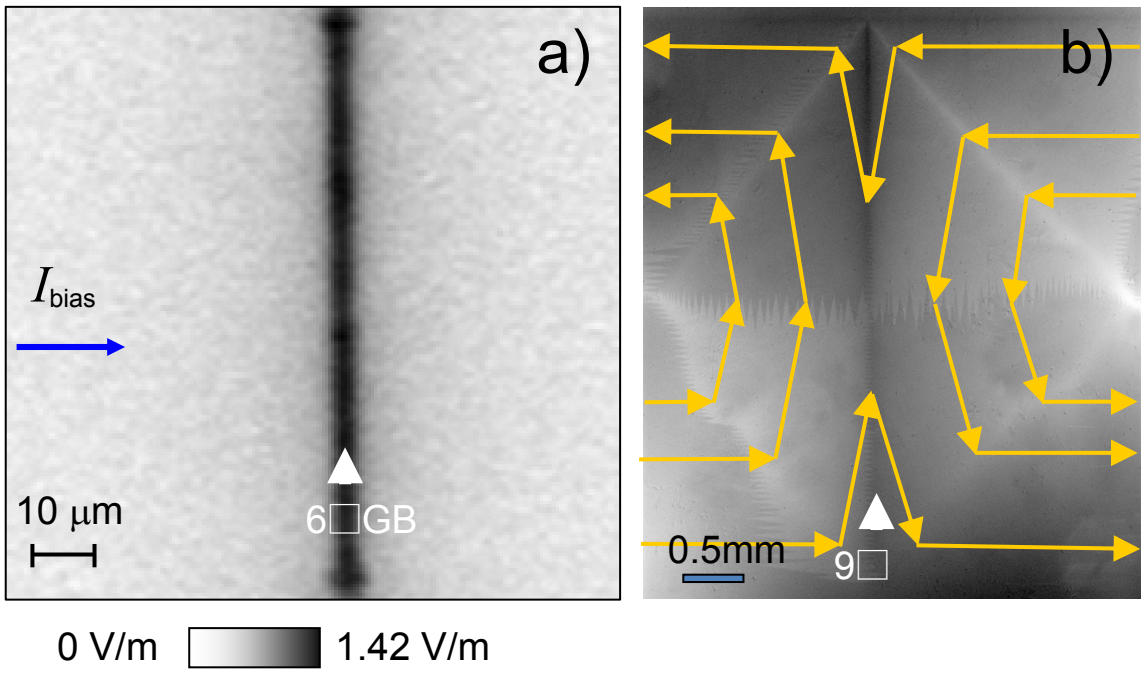

Figure IV.5. (a) Low temperature laser-scanning microscope (LTLSM) image scanned in 1 μm steps of a 6° [001] tilt bicrystal taken at 12 K in a perpendicular field of 0.25 T with bias current of 39 mA which generated 17 μV across the bridge. (a) shows a 2D map of the electric field E(x,y) induced by transport current along the 100 μm wide x 700 μm long bridge across the GB. E is enhanced by a factor of 23 at the GB as compared to the intragranular E. (b) Magneto-optical (MO) image of a 9° bicrystal with computed streamlines (yellow) of the magnetization current calculated from the Bean model [30]. The MO image was taken after cooling in a perpendicular field of 120 mT to 6 K and then reducing the field to zero. The trapped flux images shows current flow over the whole film and the streamline distortion produced by the substantial blocking effect of the GB indicates that it is a weak link. Bright lines form a rhombus and show where the current streamlines change directions in the grains due to the weak link effect of the GB. Dark contrast at the GB is caused by the reversal of the direction of the streamlines.

We performed detailed studies of the critical current densities $J_c(T,B)$ and $J_b(T,B)$ across grains and GBs for the 3°, 6°, 9° and 24° bicrystals in fields up to 16 T. Figure IV.6 shows that $J_b(12K, 0.5T)$ falls off by an order of magnitude as θ increases from 3 to 24°. This qualitative behavior is similar to $J_b(\theta)$ for [001] tilt grain boundaries in YBCO, as shown in inset. As for YBCO, the 3° GB does not obstruct supercurrent, while at higher-angles $J_b(\theta)$ becomes much smaller than the grain J_c. We do not yet have enough data in the crucial region of $9° < \theta < 30°$ to conclude if $J_b(\theta)$ drops exponentially as it does in cuprates [1], but the fact that even low angle GBs with $\theta > 6°$ do obstruct supercurrent is quite clear.

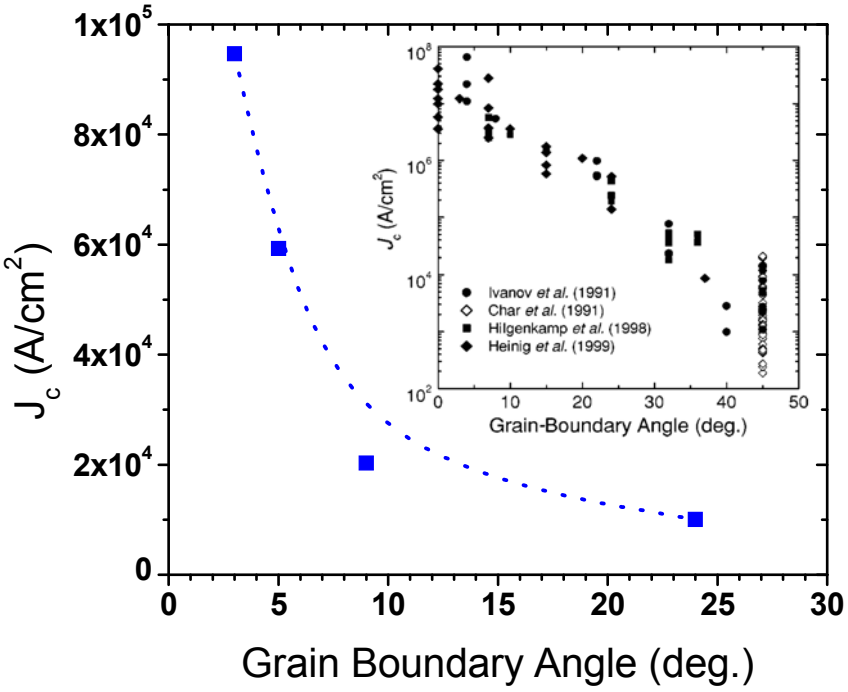

Figure IV.6. Dependence of the critical current density J_c (12 K, 0.5 T, H perpendicular to the film) as a function of the GB misorientation angle θ. The inset shows summary data from Ref. 1 for YBCO GBs. The rapid drop in $J_b(\theta)$ with increasing θ in our 122 bicrystals exhibits a similar qualitative dependence on misorientation angle, although the depression of the ratio $J_b(24°)/J_b(6°)$ in 122 appears to be somewhat less severe than in YBCO.

The field dependence of $J_b(T,H)$ shown in Figure IV.7 also exhibits a rather typical characteristic of cuprate GB transport. At low fields, $J_b(H)$ is smaller than the grain $J_c(H)$, but the difference between them diminishes as H increases, tending to make GBs lesser obstacles at higher fields. This behavior, well established for low angle YBCO bicrystals

[18-19] is described by a theory of pinning of Abrikosov-Josephson vortices on GBs and their interaction with the Abrikosov vortices within the grains [20] as illustrated in Figure IV.8

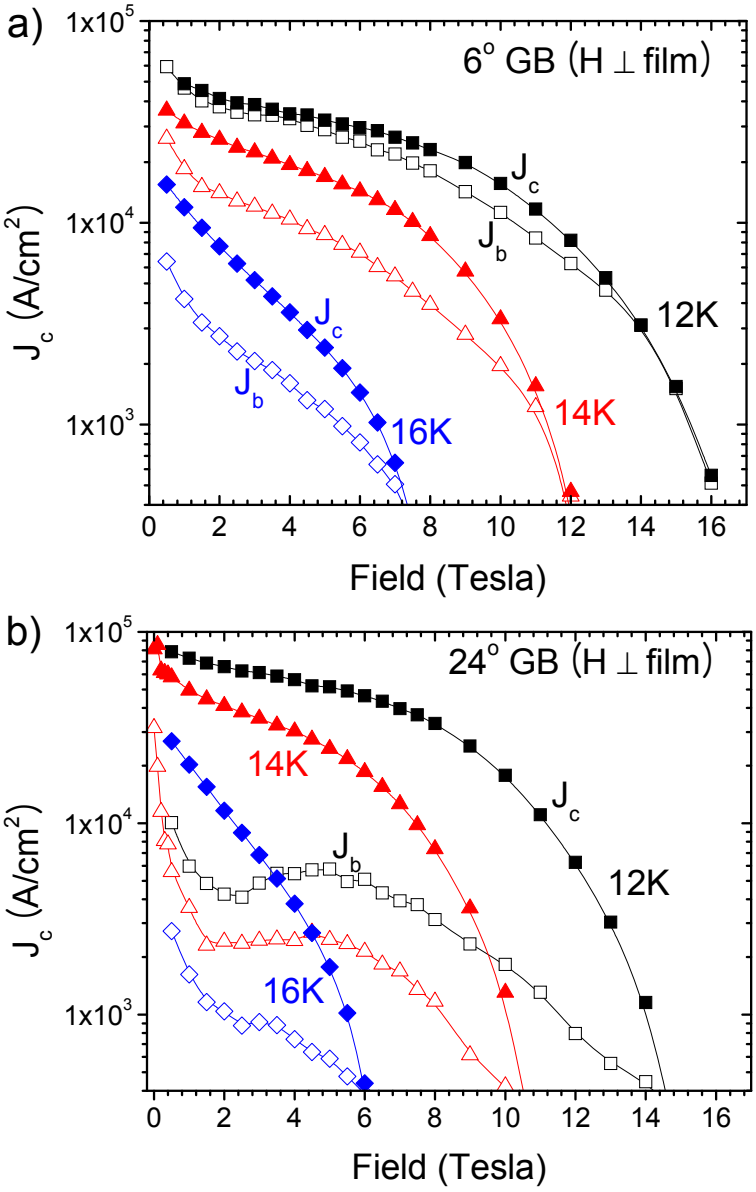

Figure IV.7. Comparative field dependencies of the critical current density across GB $J_b(H)$ and $J_c(H)$ in the grains for (a) 6° and (b) 24° bicrystals at 12K, 14K and 16K. It is clearly visible that the gap between $J_b(H)$ and $J_c(H)$ diminishes as the field increases.

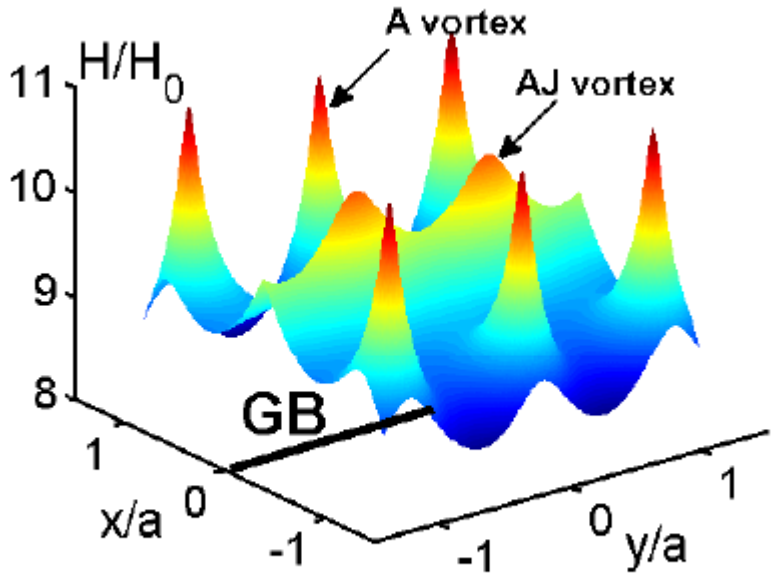

Figure IV.8. A field distribution around a vortex structure at a grain boundary calculated using the model of Ref. 20. Here $a = (\phi_0/B)^{1/2}$ is the intervortex spacing, and $H_0 = \phi_0/4\pi\mu_0\lambda^2$. The Abrikosov-Josephson (AJ) vortices on the GB have elongated Josephson cores due to the partial suppression of the superconducting order parameter at the GB. They can be pinned by both imperfections along the GB and by interaction with the Abrikosov (A) vortices in the grains. For $H < H_b$, the AJ chain can move along the boundary through the pinned A vortex structure if the current flowing across the boundary $J > J_b < J_c$. For $H > H_b$, the moving AJ chain drags neighboring A vortices, so that J_b is now limited by J_c in the grains. This mechanism explains how $J_b(B)$ can be much lower than $J_c(B)$ at low fields, while allowing a crossover of $J_b(B)$ and $J_c(B)$ at higher fields as Figure IV.7 demonstrates. The thick black line indicates the GB.

The totality of our data unambiguously indicates that GBs in 122 pnictides exhibit current-limiting behavior similar to that observed in high-T_c cuprates. The relative suppression of superconductivity at GBs at zero field in YBCO and 122 pnictides is determined by the ratio, $J_b(t)/J_d(t)$ at the reduced temperature $t = T/T_c$ where $J_d(T) = \phi_0/3^{3/2}\pi\mu_0\lambda^2\xi$ is the depairing current density, $\phi_0 = 2\times10^{-15}$ Wb is the magnetic flux quantum, λ is the London penetration depth, and ξ is the superconducting coherence length [21]. YBCO and Ba-122 have similar zero-temperature values of $\lambda(0) \sim$ 150-200 nm and $\xi(0) \sim$ 2-3 nm, as has been shown by magneto-transport measurements [10,13]. Taking, for example, $J_b \sim 10^8$ A/m^2 for a 24^o [001] tilt GB in YBCO at 77K (t = 0.84) [1] and J_d (77K) $\sim 4\times10^{11}$ A/m^2, we obtain $J_b(t)/J_d(t) \sim 2.25\times10^{-4}$. In turn, for a 24^o [001] tilt GB in Ba-122 at 16K (t = 0.76), our Figure IV.5 and 6 data give $J_b \sim 1\times10^8$ A/m^2 , and J_d (16K) $\sim 2\times10^{11}$ A/m^2 (for $\lambda(t) \sim 160(1\text{-}t)^{-1/2} \approx 330$ nm and $\xi(t) \sim 2.44(1\text{-}t)^{-1/2} \approx 4.6$ nm [13]). Thus the ratio $J_b(t)/J_d(t) \sim 5\times10^{-4}$ for the 122 pnictide turn out not to be too far apart, and somewhat larger for the 122 pnictide.

We now briefly discuss possible mechanisms underlying our results, as well as their broader implications for the ongoing search for new high T_c superconductors, starting from the fact that depression of the GB J_c implies significant depression of the superfluid density at the GB. Both for the d-wave pairing of cuprates and for the s-wave multiband pairing of pnictides [22], GB crystalline disorder depresses superconducting properties because of the short coherence length $\xi(0) \sim \hbar v_F/k_B T_c$ which quantifies the size of the Cooper pairs. The typical values of $\xi(0) \approx$ 1-2 nm extracted from H_{c2} measurements [9-13] are indeed similar for cuprates and pnictides, despite significant T_c differences. The small $\xi(0)$ of the pnictides

results from their small Fermi velocities and low carrier densities, which are even lower than the carrier densities in optimally doped cuprates. In the context of the multiband pairing scenarios of superconductivity in pnictides (see, e.g. the review [22] and references therein), depression of superconductivity at GBs could result from strong interband scattering by imperfect GB structural units or the chain of GB dislocation cores or by strain- or charge-driven Cottrell atmospheres of segregated impurities at the GB [23-25]. In pnictides where superconductivity results from strong antiferromagnetic correlations in the Fe-As planes, such GB impurity segregations may also induce local GB magnetic nanostructures, which would also contribute to order parameter depression and weak link behavior. Given the strong coupling of the superconducting order parameters in different bands inferred from *ab-initio* calculations of pnictides [22], pairbreaking interband scattering at the GB may play a much greater role in order parameter suppression than in the two-band superconductor MgB_2 in which the much weaker interband coupling and interband impurity scattering [26, 27] are consistent with the lack of weak link behavior of GBs [8]. GB weak link behavior in the pnictides may also result from strong shear strains near GB dislocation cores, which can significantly distort the local angle between Fe-As bonds from its optimal value at which T_c is maximum [28,29]. Any or all of these effects may suppress superconductivity in the channels between dislocations in low angle GBs. A further common mechanism for weak link behavior results from the generic phase diagram of cuprates and pnictides, which contains the ubiquitous superconducting “dome” around optimal doping. As in the cuprates, local compositional variations and strain and charging effects on the GB may depress the superconducting order parameter [1,21,23-25], as the superconducting state moves away from optimal doping towards the competing parent

antiferromagnetic phase. GB charging effects in the low carrier density pnictides are greatly amplified by the Thomas-Fermi screening length [21] being of the order of the coherence length**.** Certainly the HRTEM image of the 24^{o} [001] tilt GB in Figure IV.3 shows no sign of coating phases at the GB, strongly suggesting that we are indeed measuring intrinsic GB properties, unlike polycrystalline samples where wetting GB phases block current [14]. Understanding the potential for local overdoping of GBs to ameliorate GB current blocking effects in pnictides will likely be as important as in cuprates [1,23-25].

IV-5. Summary of the chapter

Our results suggest that understanding the potential for local overdoping of GBs to ameliorate GB current blocking effects in pnictides will likely be as important as in cuprates. Since the qualitative mechanisms of GB weak-link behavior discussed above may be insensitive to details of their pairing scenarios and superconducting order parameter symmetry, conditions favorable for weak-linked GBs may be present in any high-*Tc* superconductor with competing orders, short coherence length and low carrier density.

References

[1] H. Hilgenkamp *et al.*, *Rev. Mod. Phys.* ***74,*** 485-549 (2002).

[2] D. C. Larbalestier *et al.*, *Nature* ***414,*** 368-377 (2001).

[3] J. E. Durrell *et al.*, *Supercond. Sci. Technol.* ***22,*** 013001 (2009).

[4] P. N. Arendt *et al.*, *MRS Bull.* **29,** 543-550 (2004).

[5] A. Goyal *et al*., *MRS Bull.* **29**, 552-560 (2004).

[6] R. Scanlan *et al*., *Proc. of the IEEE*, **92**, 1639-1654 (2004).

[7] G. Zerweck *et al*., *J. Low Temp. Phys.* **42**, 1-9 (1981).

[8] D. C. Larbalestier *et al., Nature* **410**, 186-189 (2001).

[9] F. Hunte *et al.*, *Nature* ***453,*** 903-905 (2008).

[10] J. Jaroszynski *et al.*, *Physical Review B* ***78,*** 174523 (2008).

[11] M. M. Altarawneh *et al.*, *Phys. Rev. B* ***78,*** 220505(R) (2008)

[12] H. Q, Yuan *et al., Nature* ***457,*** 565-568 (2008).

[13] A. Yamamoto *et al.*, *Appl. Phys. Lett.,* ***94,*** 062511-062513 (2009).

[14] S. Haindl *et al*., *Phys. Rev. Lett*. **104,** 077001 (2010).

[15] A. Yamamoto *et al.*, *Supercond. Sci. Technol.* **21**, 095008 (2008).

[16] H. Hiramatsu *et al.*, *Applied Physics Express* **1**, 101702 (2008)

[17] G. Blatter *et al*., Vortex Matter In The Physics of Superconductors. Edited by K.H. Bennerman *et al*., Springer, Berlin, Heidelberg, New York, Hong Kong, London, Milan, Paris, Tokyo, **vol I** 800 (2003).

[18] D. Kim *et al.*, *Phys. Rev. B* ***62,*** 12505 (2000).

[19] D. T. Verebelyi *et al.*, *Appl. Phys. Lett.* **76**, 1755–1757 (2000).

[20] A. Gurevich *et al.*, *Phys. Rev. B* **50**, 13563-13576 (1994).

[21] A. Gurevich *et al.*, *Phys. Rev. B* **57**, 13878-13893 (1998).

[22] I. I. Mazin *et al.*, *Physica C* **469**, 614-627 (2009).

[23] M. A. Schofield *et al*., *Phys. Rev. Lett.* **92,** 195502/1-4 (2004).

[24] X. Song *et al*., *Nature Materials* **4**, 470-475 (2005).

[25] R. Klie *et al.*, *Nature* **435,** 475-478 (2005).

[26] H. J. Choi *et al*., *Nature* **418**, 758 (2002).

[27] I. I. Mazin *et al.*, *Phys. Rev. Lett.* **89,** 107002 (2002).

[28] J. Zhao *et al.*, *Nature Materials* **7**, 953-957 (2008).

[29] C. Lee *et al.*, *J. Phys. Soc. Japan* **77**, 083704 (2008).

[30] A. A. Polyanskii *et al., Phys. Rev. B* **53**, 8687-8697 (1996).

Chapter V. Artificially engineered superlattices of Co-doped $BaFe_2As_2$

V-1. The growth of Co-doped Ba-122 superlattices

Since the discovery of iron-based superconductors [1,5-9], epitaxial thin films have been successfully grown by many groups [2,10-16] and they have significantly advanced potential device applications and the understanding of the fundamental physical properties of these new superconductors [10,17-23]. In particular, we reported high quality Co-doped $BaFe_2As_2$ (Ba-122) single crystal thin films using template engineering which generated *c*-axis aligned, self-assembled, second phase nanorods [2-4] as schematized in Fig. V.1a. These nanorods yielded strong *c*-axis pinning centres that enhance the in-field critical current density, J_c. The *c*-axis pinning was so strong that actually it was able to invert the usual irreversibility field anisotropy in which H_{irr} parallel to the *ab*-plane is 1.5-2 times that parallel to the *c*-axis. This motivated us to consider using multilayer growth methods to enhance the *ab*-plane properties since high field applications prefer to enhance J_c in all field configurations, as sketched in Fig. V.1c. We note that no study of artificially controlled flux pinning for pnictide superconductor has yet been reported, while many investigations of J_c and irreversibility field (H_{irr}) enhancement by nanoparticle incorporation have been performed in the high T_c cuprate superconductor $YBa_2Cu_3O_{7-x}$ (YBCO) like that using YBCO/Y_2BaCuO_5 and YBCO/$BaZrO_3$ multilayers [24,25] On the other hand, superconducting superlattice structures (schematized in Fig. V.1b) are particularly attractive for understanding fundamental mechanisms of superconductivity and development of superconducting devices such as tunnel junctions based on pnictides.

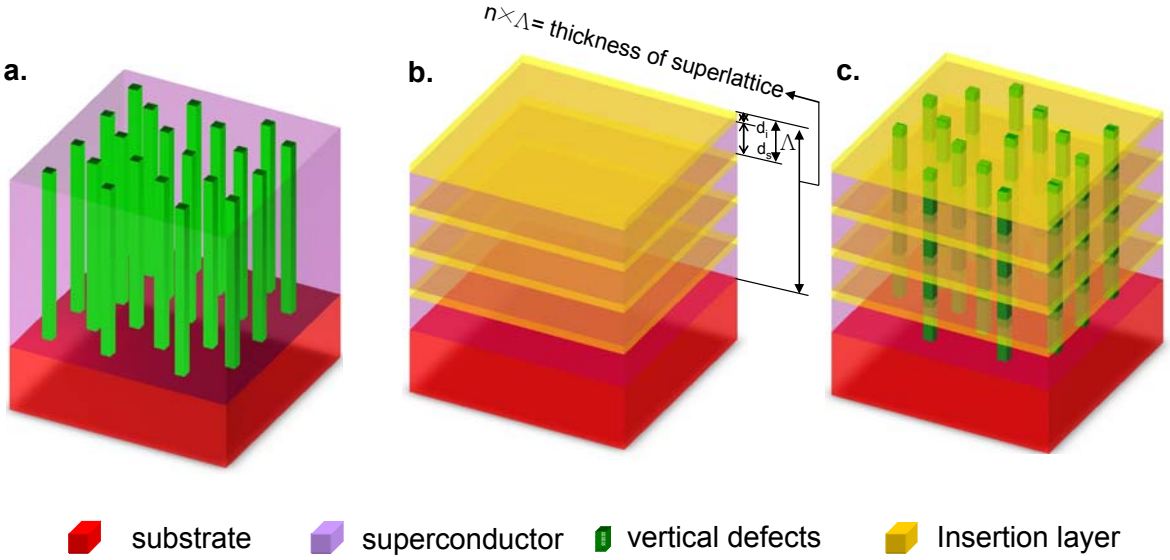

Figure V.1. Schematics of various structures of superconductor epitaxial thin films. a, superconductor thin film with defects along *c*-axis b, superlattice structure (d_i = thickness of an insertion layer, d_s = thickness of a superconductor layer, Λ (modulation wavelength) = $d_i + d_s$, n = total number of bilayers) c, superlattice structure with defects along *c*-axis

The fabrication of superlattice structures using Co-doped Ba-122 thin films is challenging because Ba-122 has metallic properties, does not contain oxygen and is easily compromised by impurities, all of which constrain the choice of interlayer. Since the first requirement is that Co-doped Ba-122 be epitaxially grown on top of the interlayer without compromising its structural and superconducting properties, the material for the interlayer must be both structurally and chemically compatible with Ba-122.

After considering detailed structural, chemical, and growth criteria, we narrowed down the possible interlayer to two different types of model superlattice structure. Since in our previous work [2], we found that a divalent, alkaline earth element-containing oxide like $SrTiO_3$ (STO) is an excellent platform on which to grow Co-doped Ba-122 thin films

due to their common features, STO was our first choice. This led to a structurally modulated superlattice with sharp interfaces, devoid of *c*-axis defects. The second choice of interlayer was undoped Ba-122 made from an oxygen-rich, Co-free 122 target (O-Ba-122) where the interlayer has a similar structure but slightly different lattice parameter. This led to compositionally modulated O-Ba-122 / Co-doped Ba-122 superlattice. Our hypothesis was that oxygen-rich, undoped Ba-122 would facilitate the formation of strong pinning, oxygen-rich precipitates along the *ab*-planes, just as it had for the *c*-axis pins in single layer films of Co-doped Ba-122.

With this approach, we have successfully grown epitaxial superlattices of $STO_{1.2\ nm}$ / 8 % Co-doped Ba-$122_{13\ nm}$ and O-Ba-$122_{3\ nm}$ / 8 % Co-doped Ba-$122_{13\ and\ 20\ nm}$ on 40 nm STO templates deposited on (001) $(La,Sr)(Al,Ta)O_3$ (LSAT) single-crystal substrates by using pulsed laser deposition. We varied the thickness of the bilayer (modulation wavelength = Λ) and the total number of bilayers (n). Their structural and superconducting properties are listed in Table V.1. To focus on the key points, we discuss here only ($STO_{1.2\ nm}$ / Co-doped Ba-$122_{13\ nm}$) × (n=24) superlattice (hereafter referred to as STO SL) and (O-Ba-$122_{3\ nm}$ / Co-doped Ba-$122_{13\ nm}$) × (n=24) superlattice (hereafter referred to as O-Ba-122 SL).

Table V.1. Crystalline quality and superconducting properties of various ($STO_{x\ nm}$ / Co-doped Ba-$122_{y\ nm}$ and O-Ba-$122_{x\ nm}$ / Co-doped Ba-$122_{y\ nm}$) × n superlattices. As a comparison, the properties of single layer Co-doped Ba-122 thin film are also shown. FWHM of rocking curves of Co-doped Ba-122 (004) reflections are shown as measures of

the crystalline quality. T_c, $\rho=0$, ΔT_c, and magnetization J_c characterize the superconducting properties.

Co-doped Ba-122 thin films on	FWHM $\Delta\omega$ (°)	$T_{c,\rho=0}$ (K)	ΔT_c (K)	J_c (4.2K, SF) (MA/cm^2)	J_c (4.2K, 10T) (MA/cm^2)
($STO_{1.2\ nm}$/ Co-doped Ba-$122_{13\ nm}$)X24	0.97	17.0	2.0	3.39	0.051
(O-Ba-$122_{3\ nm}$/ Co-doped Ba-$122_{13\ nm}$)X16	0.27	22.3	0.9	3.73	0.296
(O-Ba-$122_{3\ nm}$/ Co-doped Ba-$122_{13\ nm}$)X24	0.26	22.9	1.0	3.20	0.300
(O-Ba-$122_{3\ nm}$/ Co-doped Ba-$122_{20\ nm}$)X16	0.35	22.4	1.0	3.35	0.233
(O-Ba-$122_{3\ nm}$/ Co-doped Ba-$122_{20\ nm}$)X24	0.31	22.5	1.3	3.44	0.263
Single layer Co-doped Ba-122	0.55	20.5	1.9	2.90	0.596

V-2. Crystalline quality of Co-doped Ba-122 superlattices

The epitaxial crystalline quality and modulation wavelength (Λ) of the superlattices were determined by four-circle x-ray diffraction (XRD) with a Cu K_α source (λ = 1.5405 Å). Figure V.2a shows the θ-2θ scan of the STO SL. The XRD pattern shows that Co-doped Ba-122 00*l* reflections dominate, which indicates *c*-axis epitaxial growth normal to the STO template and LSAT substrate. Figure V.2c is a magnification of Fig. V.2a close to the 002 reflection of the STO SL which clearly shows satellite peaks with calculated modulation length Λ = 14 nm ± 2 nm the same as the nominal Λ. Rocking curves for the 004 reflection were measured to determine the out-of-plane mosaic spread and crystalline quality. As shown in Fig. V.2d, the full width at half maximum (FWHM) of the 004 reflection rocking curve of STO SL is 0.97°. Furthermore, the STO SL exhibits strong and sharp peaks ($\Delta\phi$ = 1.1°) only every 90° in the azimuthal phi scan of the off-axis 112

reflection of Co-doped Ba-122 **(**Fig. V.3a**)** revealing a good in-plane epitaxy. These results confirm the excellent epitaxial arrangement, even though as many as 24 STO / Co-doped Ba-122 bi-layers were grown.

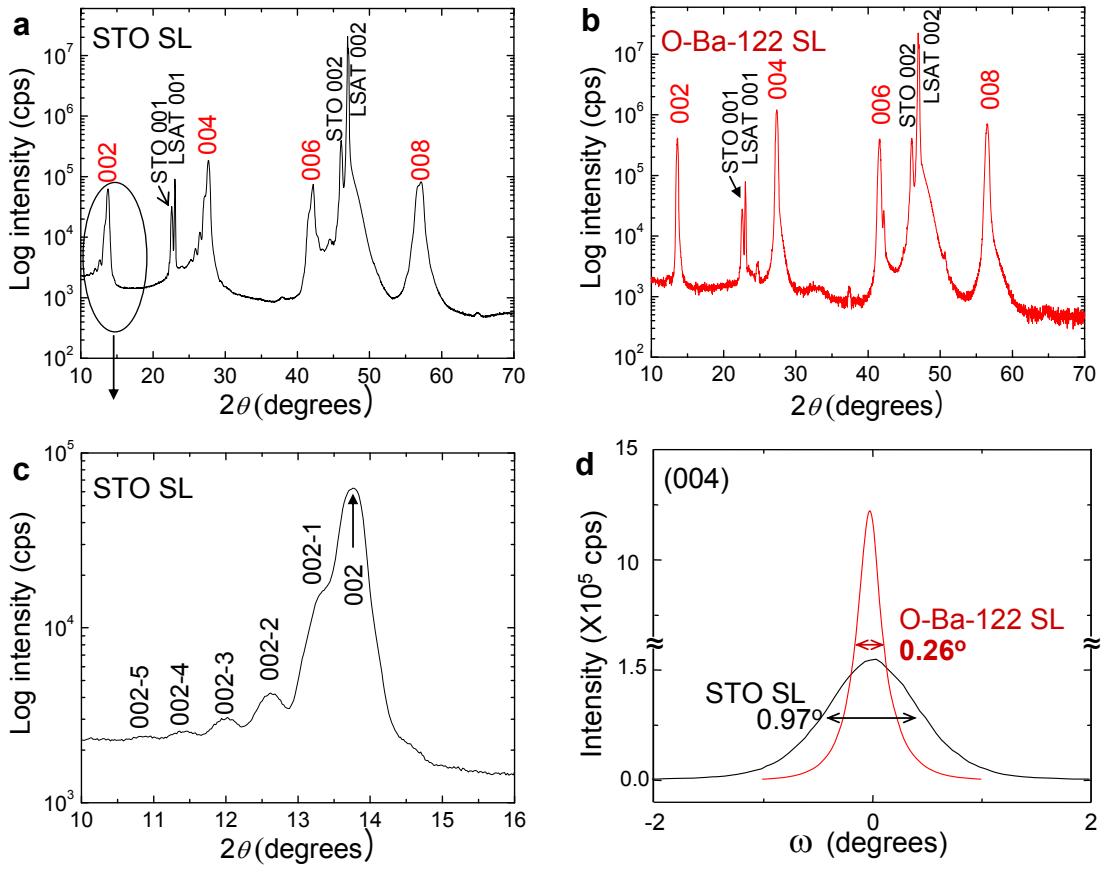

Figure V.2. XRD patterns obtained on O-Ba-122 inserted and STO inserted Co-doped $BaFe_2As_2$ superlattices. a, Out-of-plane θ-2θ XRD pattern of ($STO_{1.2\ nm}$/Co-doped Ba-$122_{13\ nm}$)×24. b, Out-of-plane θ-2θ XRD pattern of (O-Ba-$122_{3\ nm}$/Co-doped Ba-$122_{13\ nm}$)×24. c, Magnified at near 002 reflection of ($STO_{1.2\ nm}$/Co-doped Ba-$122_{13\ nm}$)×24. d, Rocking curves and FWHM for (004) reflection of two superlattices.

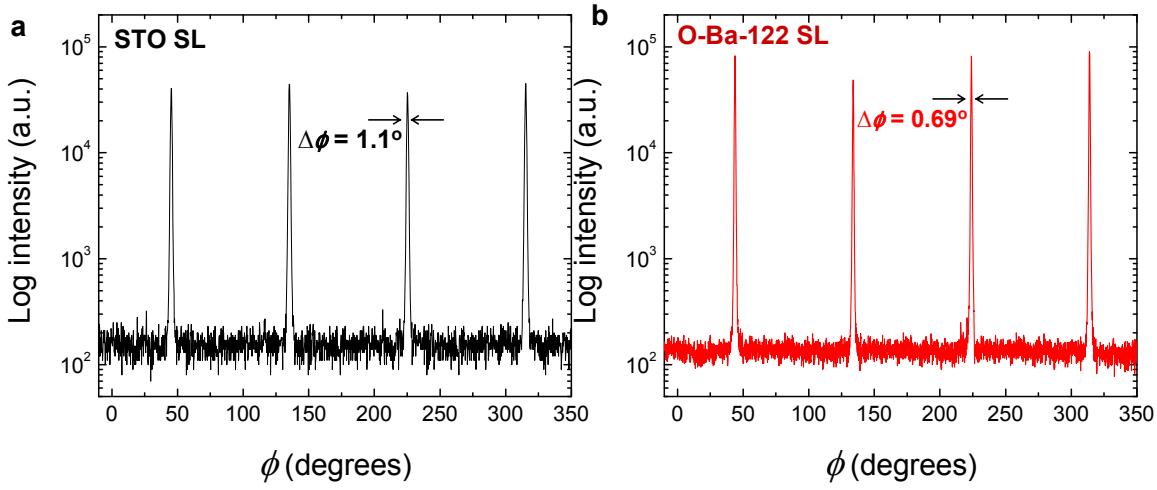

Figure V.3. Azimuthal ϕ scan and $\Delta\phi$ of the off-axis 112 reflection of a, ($STO_{1.2\ nm}$/Co-doped Ba-$122_{13\ nm}$)×24. b, (O-Ba-$122_{3\ nm}$/Co-doped Ba-$122_{13\ nm}$)×24 superlattices

Figure V.2b is the θ-2θ scan of the O-Ba-122 SL and it shows excellent *c*-axis epitaxial growth. Fig. V.2d shows the FWHM of the 004 reflection rocking curve of O-Ba-122 SL to be as narrow as 0.26°, which is far superior to the STO SL and even better than other reports about single layer Ba-122 thin films [15,18]. Furthermore, as shown in Fig.V.3, the azimuthal phi scan of O-Ba-122 SL shows much sharper peaks ($\Delta\phi$ = 0.69°) than the STO SL. The reason why O-Ba-122 SL has superior crystalline quality is that O-Ba-122 and Co-doped Ba-122 are structurally identical, differing only by the 8% cobalt addition. Since the atomic scattering factors of Co and Fe are very close it would be exceedingly difficult to see any satellite peaks by x-ray diffraction.

V-3. Microstructure of Co-doped Ba-122 superlattices

To investigate the microstructure of STO and O-Ba-122 SLs, transmission electron microscopy (TEM) was used. Figure V.4a, b show cross sectional low and high magnification high-angle annular dark field (HAADF) images of STO SL. In Fig. V.4a, bright and dark layers correspond to 13 nm Co-doped Ba-122 layer and 1.2 nm STO layer, respectively. We can clearly see that there are 24 STO / Co-doped Ba-122 bi-layers and Λ is 14 nm in accordance with our design and the modulation wavelength determined by x-ray diffraction. Furthermore, 3 unit-cell-thick STO interlayers have been uniformly grown on the Co-doped Ba-122 layer as shown in Fig. V.4b. This indicates that we can control the thickness of the STO interlayer with single unit-cell precision and maintain an atomically sharp interface between STO and Co-doped Ba-122. A schematic of the <100> projection of Co-doped Ba-122 and STO at the interface is shown to the right of Fig. V.4b, where the bonding of the FeAs layer to the SrO layer in STO is quite evident, in excellent agreement with the hypothesis we previously proposed [2].

Figure V.4c is a cross-sectional TEM image of the O-Ba-122 SL, which clearly shows 24 bilayers and the modulation wavelength Λ=16 nm. The planar view TEM images (Figure V.4d) exhibits *c*-axis aligned defects as we observed in the single layer Co-doped Ba-122 in our previous reports [2,3]. The first interesting point is that the interface O-Ba-122 layers have grown as laterally aligned but discontinuous second phase nano particles of several nm size. Presumably, island growth of the oxygen-containing second phase is energetically favourable due to the small lattice mismatch with the Co-doped Ba-122 SL. Similar discontinuous growth was observed with $YBa_2Cu_3O_7$/ YBa_2CuO_5 multilayers [24]. The second interesting point is that the O-Ba-122 SL has *c*-axis defects extending across many *ab*-axis aligned nano particle arrays, while the STO SL does not have such *c*-axis

aligned defects. We infer that oxygen which is needed to produce the *c*-axis aligned defects is absorbed by the STO interlayers under our high-vacuum, high-temperature growth conditions. The structure of the O-Ba-122 SL is thus akin to Fig. V.1c which is more desirable than the structure of the STO SL (Fig. V.1b) for flux pinning, since the O-Ba-122 SL has structural defects in both *c*- and *ab*-axis directions. Strictly speaking, the actual morphology of O-Ba-122 SL is close to Fig. V.1c with nanoparticles rather than a continuous bilayer interface.

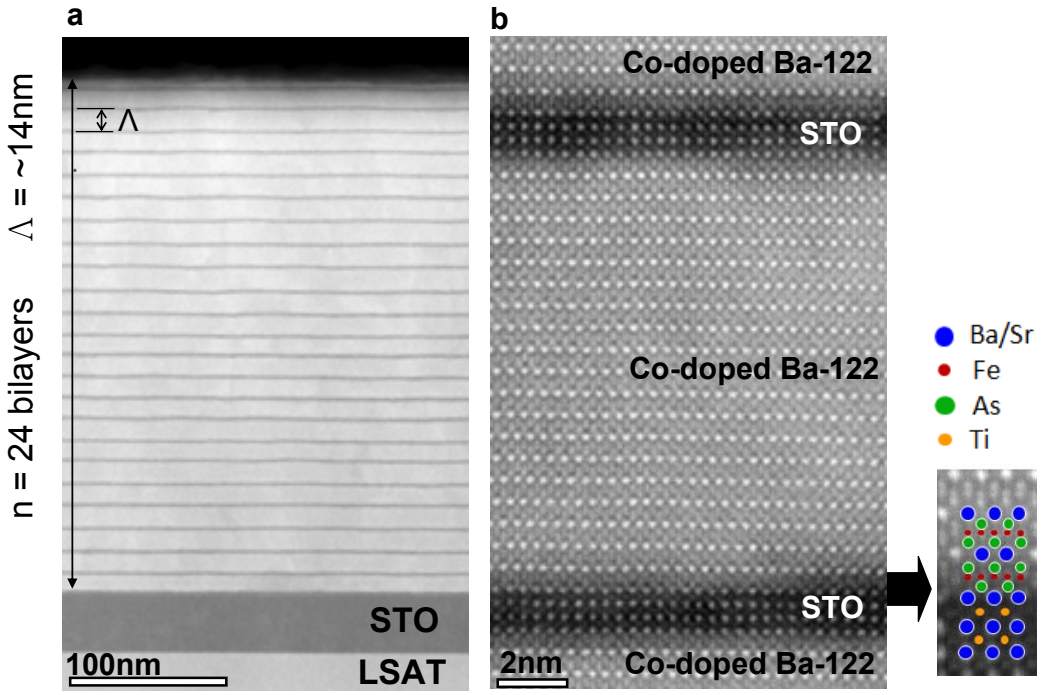

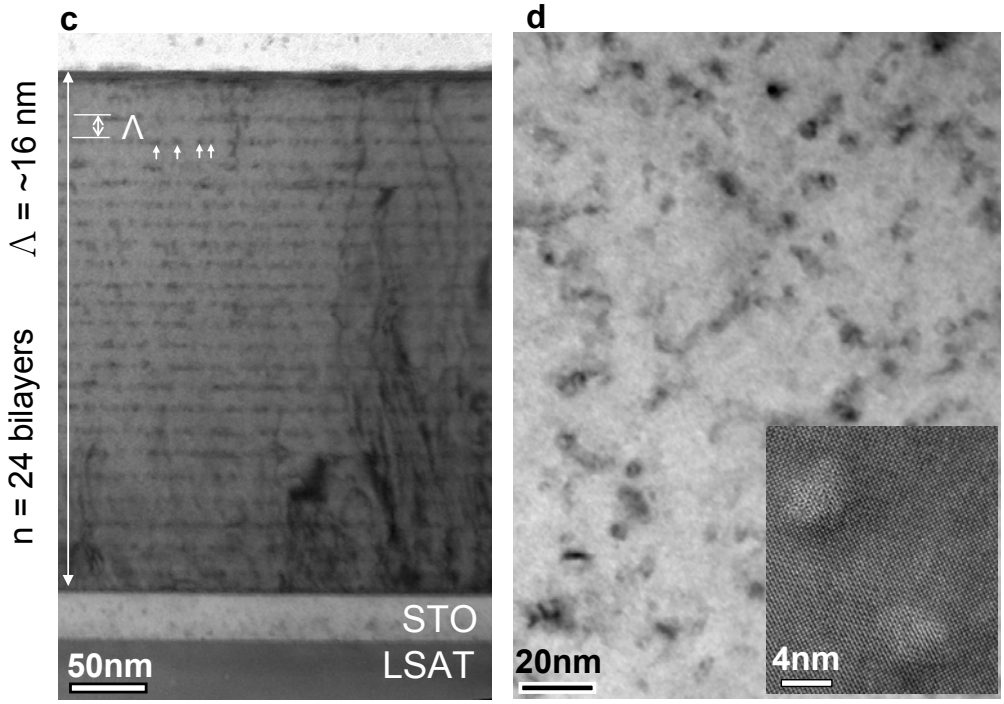

Figure V.4. Microstructure of Co-doped $BaFe_2As_2$ superlattices thin films investigated by TEM. a-b, HAADF image of the <100> projection of ($STO_{1.2\ nm}$/Co-doped Ba-$122_{13\ nm}$)×24. **c**, Cross-sectional TEM image of the <100> projection of (O-Ba-$122_{3\ nm}$/Co-doped Ba-$122_{13\ nm}$)×24. Arrows indicate nano particle arrays in the O-Ba-122 layer along *ab*-axis. d, Planar view TEM image of (O-Ba-$122_{3\ nm}$/Co-doped Ba-$122_{13\ nm}$)×24 showing vertical defects along *c*-axis. Inset shows the high resolution image of vertical defects.

V-4. Superconducting properties of Co-doped Ba-122 superlattices

To characterize the superconducting transition temperature T_c, resistivity was measured as a function of temperature (ρ-T) by the van der Pauw method. As shown in Fig. V.5, the residual resistivity ratio (RRR) of the O-Ba-122 SL (1.7) is slightly lower than that of the STO SL (2.2). In the inset of Fig. V.5, O-Ba-122 SL shows high $T_{c,\ \rho=0}$ = 22.9 K, and

narrow ΔT_c of 1.1 K, which indicates the good quality of these layered films even in the presence of significant lateral second phase. By contrast, $T_{c,\,\rho=0}$ of the ultrathin layers of STO SL is suppressed to 17.0 K. Evidently, compatibility between the O-Ba-122 and Co-doped Ba-122 is better than that between STO and Co-doped Ba-122. Figure V.5 also indicates a $T_{c,\,\rho=0}$ of 20.5 K for ~400 nm thick single layer Co-doped Ba-122 film deposited on 40 nm STO/LSAT.

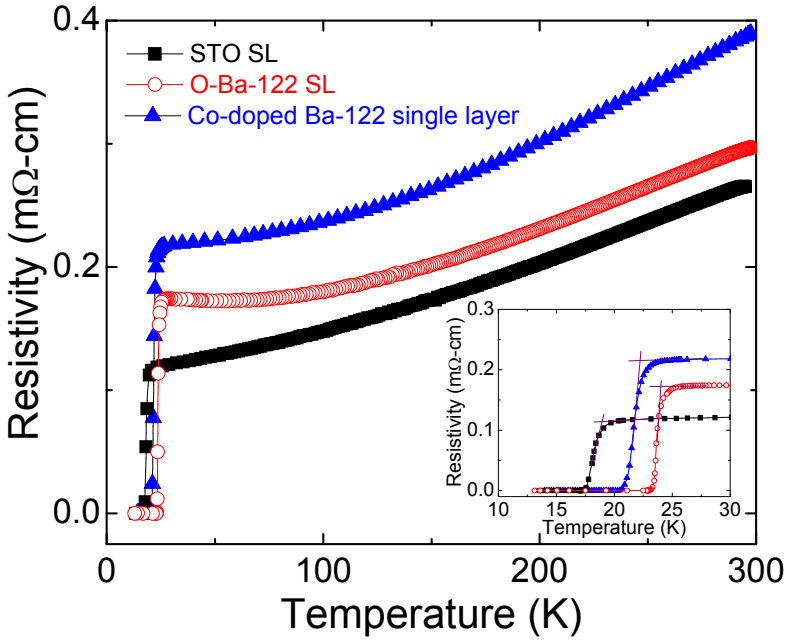

Figure V.5. Resistivity as a function of temperature. ρ(T) from room temperature to below T_c. Inset figure is superconducting transition of all films.

In order to understand the effect of this nanostructural engineering on J_c and H_{irr} we made extensive characterizations at various temperatures, fields and field orientations to the crystal axes. Figure V.6a shows $J_c(H)$ for $H//c$ at 4.2K far from T_c . It is immediately clear that the two samples with c-axis nanorod pinning defects have much higher $J_c(H)$ and

$H_{irr}(T)$. The influence of the *ab*-plane defects is revealed in Fig. V.6b where the J_c anisotropy for the O-Ba-122 SL and Co-doped Ba-122 single layers at 16K for perpendicular ($H//c$) and parallel ($H//ab$) configurations is compared. Despite these data being affected by their T_c differences (the O-Ba-122 SL has a higher T_c, consistent with its higher J_c), both samples have the same H_{Irr}~11T for H parallel to the *c*-axis, a result consistent with the lower density of *c*-axis pinning centres in O-Ba-122 SL compared to the single layer Co-doped Ba-122. But the really striking result is that the inverted H_{irr} anisotropy seen for the single layer film with only *c*-axis defects (H_{irr} for $H//ab$ is less than for $H//c$) is corrected when *ab*-plane pins are present in the O-Ba-122 SL film. It is clear that H_{irr} for $H//ab$ ($H_{irr,ab}$) of O-Ba-122 SL is approximately doubled from 9 to ~19 T, restoring the expected anisotropy of H_{irr} and $J_c(H)$ without any degradation to the *c*-axis properties. This enhancement is due to the presence of the *ab*-plane aligned nanoparticles in the O-Ba-122 SL shown in Fig. V.4.

The angular transport J_c of the STO SL, O-Ba-122 SL, and Co-doped Ba-122 single layer [2-4] shown in Fig. V.6c evaluated at a constant reduced temperature T/T_c ~0.6 provides further insight into the pinning effects of the nanoparticles. The Co-doped Ba-122 single layer [2-4] shows only the strong *c*-axis pinning produced by the correlated, self-assembled nanopillars, while the J_c of the STO SL shows only a sharp, few-degrees wide peak when the magnetic field is aligned with the *ab*-plane STO superlattice. The $J_c(\theta)$ of O-Ba-122 SL is higher than the other two samples and shows both strong *ab*-plane and *c*-axis peaks, which is quite consistent with the *ab*-plane aligned second-phase nanoparticles of

the bilayer and its *c*-axis aligned defects, seen in Fig. V.4c and d. Very strong pinning in fields up to 45 T will be reported elsewhere [26].

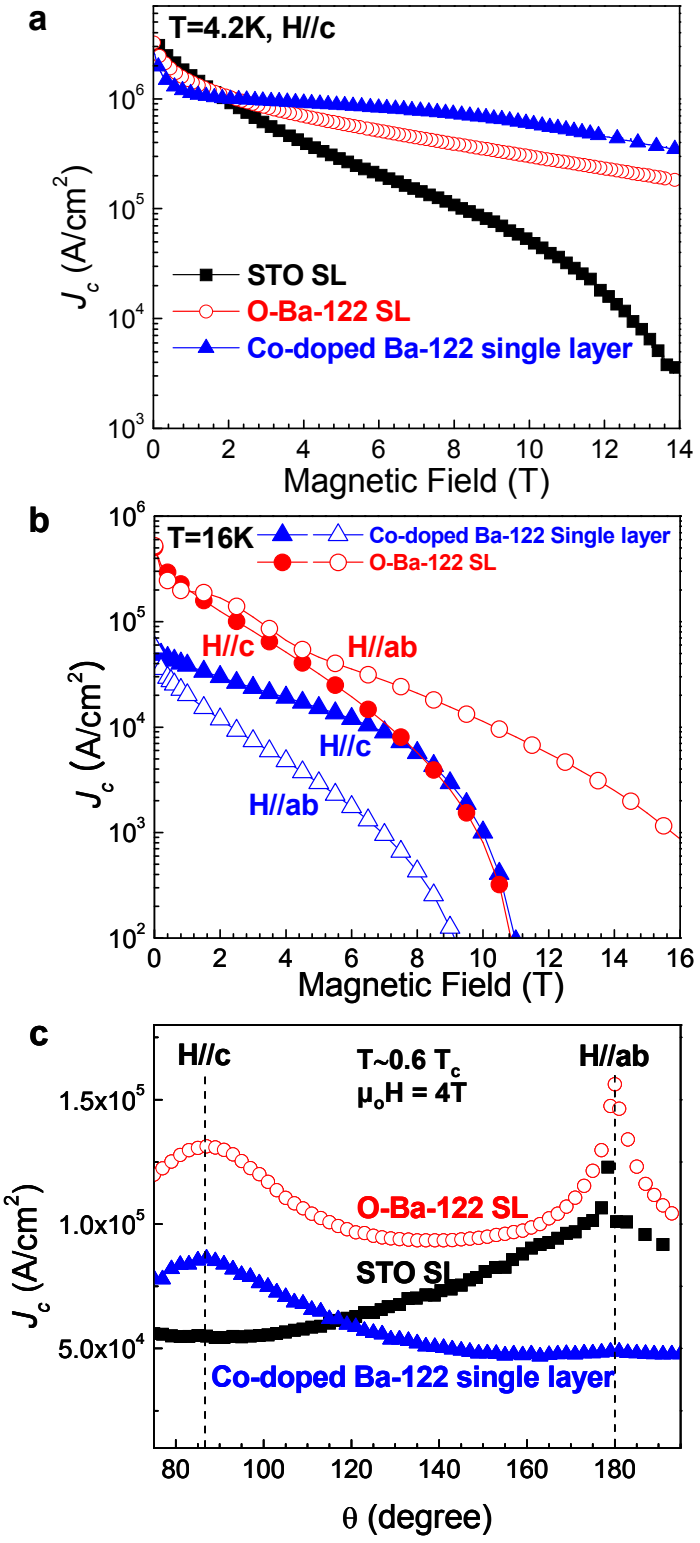

Figure V.6. J_c as a function of magnetic field. a, Magnetization J_c as a function of magnetic field at 4.2K with the field applied perpendicular to the plane of all three films. b, Transport J_c as a function of magnetic field at 16K with the field applied perpendicular and parallel to the plane of (O-Ba-$122_{3\ nm}$/Co-doped Ba-$122_{13\ nm}$)×24 and Co-doped Ba-122 single layer thin films. c, Angular dependence of transport J_c at 4T for all three films at a reduced temperature of T/T_c = ~0.6.

V-5. Summary of the chapter

In summary, we have grown artificially layered superlattice structures in Co-doped Ba-122 thin films with controlled structural and compositional modulations. The insertion of undoped Ba-122 layers allows nanoparticle formation that introduces strong vortex pinning along the *ab*-planes while still allowing the formation of vertically-aligned defects. The remarkable enhancement of the pinning properties over a wide angular range related to the *ab*-plane nanoparticles is highlighted by the significant increase of the irreversibility field and by much improved J_c. The engineered structures presented here are surely capable of further refinement by optimizing interlayer separation and the composition of the vortex pinning layers features which cannot be obtained in single layer films. The successful growth of such high quality artificially layered structure will have wide implications for achieving new interface-driven high T_c superconductivity [27] and potential device applications involving SNS and SIS junctions [28] Furthermore, artificially made multilayer structures can also be used as model systems to study many physical phenomena such as dimensionality, proximity effect and interface pinning.

References

[1] Y. Kamihara, *J. Am. Chem. Soc.* **130**, 3296–3297 (2008).

[2] S. Lee *et al*., *Nature Mater.* **9,** 397 (2010).

[3] Y. Zhang *et al. Appl. Phys. Lett*. **98**, 042509 (2011).

[4] C. Tarantini *et al. Appl. Phys. Lett*. **96**, 142510 (2010).

[5] X. H. Chen *et al*., *Nature* **453**, 761 (2008).

[6] C. Wang *et al*., *Euro Phys. Lett*., **83,** 67006 (2008).

[7] M. Rotter *et al*., *Phys. Rev. Lett*. **101,** 107006 (2008).

[8] A. S. Sefat *et al*., *Phys. Rev. Lett*. **101,** 117004 (2008).

[9] F.-C. Hsu *et al*., *Proc. Natl. Acad. Sci. USA* **105,** 14262 (2008).

[10] S. Lee *et al., Appl. Phys. Lett.* **95**, 212505 (2009).

[11] T. Katase *et al., Appl. Phys. Express* **3**, 063101 (2010).

[12] S. Haindl *et al.*, *Phys. Rev. Lett.* **104**, 077001 (2010).

[13] T. Kawaguchi *et al.*, *Appl. Phys. Lett.* **97**, 042509 (2010).

[14] K. Iida *et al., Appl. Phys. Lett.* **97**, 172507 (2010).

[15] T. Katase *et al., Nat. Commun.* **2**, 409 (2011).

[16] K. Iida *et al., Appl. Phys. Express* **4**, 013103 (2011).

[17] S. Baily *et al., Phys. Rev. Lett.* **102**, 117004 (2009).

[18] T. Katase *et al.*, *Appl. Phys. Lett.* **96**, 142507 (2010).

[19] M. Mehta *et al., Appl. Phys. Lett.* **97**, 012503 (2010).

[20] A. Perucchi *et al.*, *EPJ B* **77**, 25–30 (2010).

[21] G. Sheet *et al., Phys. Rev. Lett.* **105**, 167003 (2010).

[22] R. V. Aguilar *et al., Phys. Rev. B* **82**, 180514 (2010).

[23] J. Yong *et al., Phys. Rev. B* **83**, 104510 (2011).

[24] T. Haugan *et al., Nature* **430**, 867–870 (2004).

[25] A. Kiessling *et al.*, *Supercond. Sci. Technol.* **24**, 055018 (2011).

[26] C. Tarantini *et al.,* In preparation.

[27] A. Gozar *et al., Nature* **455**, 782–785 (2008).

[28] M. Covington *et al., Phys. Rev. Lett.* **79**, 277–280 (1997).

Chapter VI. Strain effect on T_c of Co-doped $BaFe_2As_2$

VI-1. Thermal expansion mismatch between Co-doped Ba-122 and CaF_2

Since the discovery of iron based superconductor (FeSC) [1-6], it has attracted significant attention and resulted in enormous studies for understanding the fundamental physics and improving superconducting properties from the application point of view [7-15]. Elevating superconducting transition temperature (T_c) is one of the most important and interesting studies [2,3]. In early stages, rare-earth (RE) 1111 shows increase of T_c by applying chemical pressure with changing rare-earth cations [2,3]. Also, there are many systematic studies about the effect of the pressure to FeSC, which revealed that applied hydrostatic pressure to bulk parent materials of RE-1111 and alkaline-earth (AE) 122 could generate superconductivity and increase T_c [16-20].

Pressure effect could be studied by other manner. Strained epitaxial thin films could be used for the study about the effect of biaxial compressive or tensile strain on T_c along *a* and *b* crystallographic direction. There was rapid progress about the growth of FeSC epitaxial thin films on various substrates by the pulsed laser deposition (PLD) or the molecular beam epitaixy (MBE) [7,21-28] and some groups reported the strain effect on the T_c of various FeSC family such as 11, RE-1111, AE-122 phases [26,29-31]. Indeed, several investigations about 11 and RE-1111 showed that T_c of strained thin films exceeded maximum T_c of bulk material based on phase diagram but reported T_c of strained AE-122 thin films is still lower than that [29-31].

Our previous study shows that high quality Co-doped Ba-122 epitaxial thin films could be grown on thin $SrTiO_3$ (STO) templated $(La,Sr)(Al,Ta)O_3$ (LSAT) in our growth

condition [21]. We believe it is due to the common factor between STO and Ba-122. The common factor means that both of materials include alkaline-earth, divalent elements such as Sr and Ba. The films show superior quality in terms of both crystalline and superconducting properties but the T_c is always lower than bulk by 3~4K [21]. Furthermore, even though the lattice constant of STO/LSAT is 3.868 Å which means lattice mismatch with Co-doped Ba-122 is -2.6%, always grown films were fully relaxed using our growth condition.

To grow strained Ba-122 epitaxial thin flims, we considered the thermal expansion mismatch engineering. The thermal expansion coefficient (α) of perovskite oxide substrates such as STO and LSAT is ~10×10^{-6} /K at 300K which is almost same as Co-doped Ba-122 (8×10^{-6} /K at 300K along *a, b* direction) [32]. So, we searched for other possible substrate which has much higher α than Co-doped Ba-122, common factor like STO, and lattice constant compatible with Co-doped Ba-122. Among the materials including divalent alkaline-earth element, CaF_2 was chosen. The lattice constant of cubic CaF_2 is 5.463 Å so the d-spacing of [220] plane is 3.863 Å, which is comparable with Co-doped Ba-122 (3.964 Å) by lattice mismatch of -2.6%. Furthermore, α of CaF_2 is ~18.7×10^{-6} /K at 300K which is much higher than Co-doped Ba-122 by more than 2 times.

In this chapter, we report highest T_c among Co-doped Ba-122 epitaxial thin films even higher than maximum T_c of bulk obtained by thermal expansion mismatch engineering. The epitaxial thin films that we grew shows T_c at zero resistivity ($T_{c,\rho=0}$) is 26.7K. Furthermore, critical current density (J_c) is as high as ~5MA/cm^2 at self field, which is comparable to our previous reported high quality epitaxial thin films [21]. We grew ~330nm-thick Co-doped Ba-122 on both (001) CaF_2 and ~40nm-thick STO / LSAT by

pulsed-laser deposition (PLD) using KrF excimer laser (248 nm) in a vacuum of 3×10^{-4} Pa at 730 ^{o}C. The Co-doped Ba-122 target was prepared by solid-state reaction with a nominal composition of Ba : Fe : Co : As = 0.98 : 1.84 : 0.16 : 2.1. Structural and superconducting properties of these films are measured by four-circle x-ray diffraction (XRD), transmission electron microscopy (TEM), four point electrical transport measurement, zero filed cooling, and oxford vibrating sample magnetometer (VSM).

VI-2. Structural properties of Co-doped Ba-122 thin films grown on CaF_2 substrate

Figure VI.1a shows the out-of-plane θ-2θ scans of the films on STO / LSAT and CaF_2. The XRD patterns show only the film 00*l* reflections, which indicates *c*-axis growth normal to the template and substrate. Rocking curves for the 004 reflection were measured to determine the out-of-plane mosaic spread and crystalline quality. The full width at half maximum (FWHM) of the 004 reflection rocking curve of the films on STO/LSAT and CaF_2 are as narrow as 0.34^{o} and 0.49^{o}, which is comparable with our previous work. Also, in-plane texture and epitaxial quality were determined by azimuthal ϕ scans of the off-axis (112) peak, as shown in Fig. VI.1b. Both films show only sharp, strong peaks every 90^{o} and $\Delta\phi$ were as narrow as 0.77^{o} (on STO / LSAT) and 0.58^{o} (on CaF_2), respectively. It means that both films show the characteristic of a truly epitaxial with perfect in-plane texture. The only noticeable difference between two films is the 2θ position

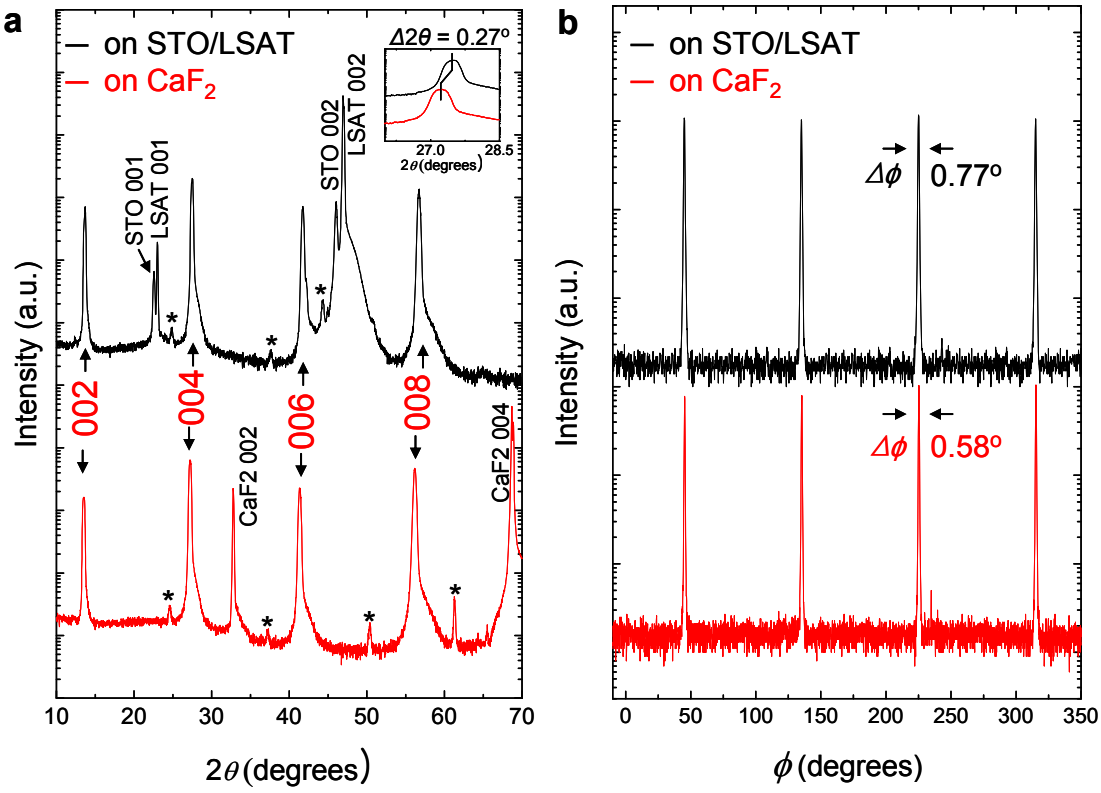

Figure VI.1. Crystalline structure examined by XRD measurement.

a, Out of plane XRD scan of Co-doped Ba-122 thin films grown on STO/LSAT and CaF_2. In-set shows magnified scan at near the 004 reflection of Co-doped Ba-122 thin films grown on STO/LSAT and CaF_2

b, Azimuthal ϕ scan of 112 off-axis reflection of Co-doped Ba-122 thin films grown on STO/LSAT and CaF_2. Small peaks notated by star(*) are reflections of identified peaks resulting from CuKβ.

of 00*l* reflections. In-set of Fig. VI.1a shows the magnified scan at near 004 reflections of both films, which clearly show that film grown on CaF_2 have lower 2θ value than films

grown on STO / LSAT by 0.27°. It means that *c* lattice constant of film grown on CaF_2 (13.090 Å) is longer than that of film grown on STO / LSAT (12.965 Å). Also, we found that in-plane lattice constants were 3.933 Å for the film grown on CaF_2 and 3.963 Å for the film grown on STO / LSAT, respectively. Compared with bulk single crystal values (a = b = 3.964 Å and c = 12.980 Å), films grown on STO / LSAT are fully relaxed but on CaF_2 has biaxial compressive strain along *a, b* direction. CaF_2 substrate could shrink ~0.05Å along a, b direction from 730°C which is Ba-122 growth temperature to room temperature based on the calculation using $\alpha = \sim 18.7 \times 10^{-6}$ /K. If the Co-doped Ba-122 thin films could shrink by clamping with CaF_2 substrate, the value might be 3.935Å which is well matched with the value we obtained by XRD analysis. So we believe that the compressive strain of Co-doped Ba-122 on CaF_2 is due to the thermal expansion mismatch.

To verify the crystalline quality, microstructures were studied by transmission electron microscopy (TEM). Figures VI.2a-b show the cross-sectional TEM images of the films grown on CaF_2. Figure VI.2a shows the interface and we can clearly see that the Ba layer in Ba-122 bonds to the F layer in CaF_2 which could be predicted by our previous work [21]. Figure VI.2b shows one arsenic layer missed stacking fault in the initial layers of Co-doped Ba-122 films. We believe that the initial stage of the film during high temperature growth of 730°C, volatile arsenic might not bond well so such defects could be generated. However, we barely see defects in thicker region which means that the crystallization becomes stable during the growth.

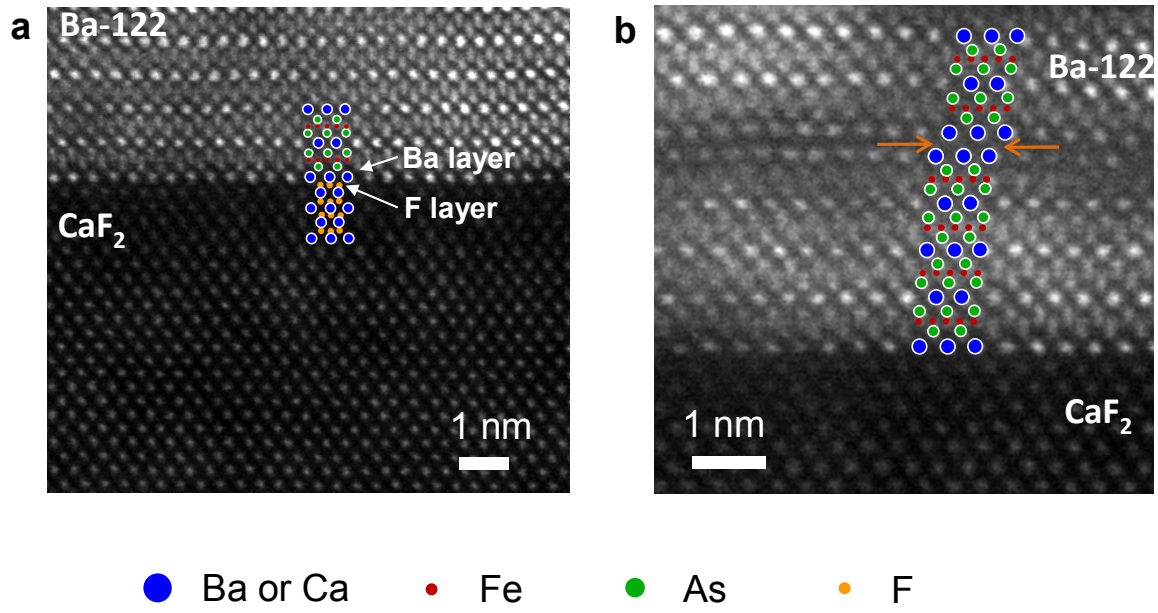

Fig VI.2. Cross sectional TEM image of Co-doped Ba-122 thin films grown on CaF_2

a) Interface between CaF_2 substrate and Co-doped Ba-122 thin film

b) Stacking fault by missing As at the initial Co-doped Ba-122 thin film layers

VI-3. Superconducting properties of Co-doped Ba-122 thin films grown on CaF_2 substrate

To characterize the superconducting transition temperature T_c, resistivity was measured as a function of temperature (ρ-T) by the van der pauw method. As shown in-set of Fig. VI.3a, the residual resistivity ratio (RRR) of the Co-doped Ba-122 film grown on STO/LSAT and CaF_2 is ~ 2.1 and 1.9, respectively, values characteristic of Co-doped Ba-122 single-crystals [5].

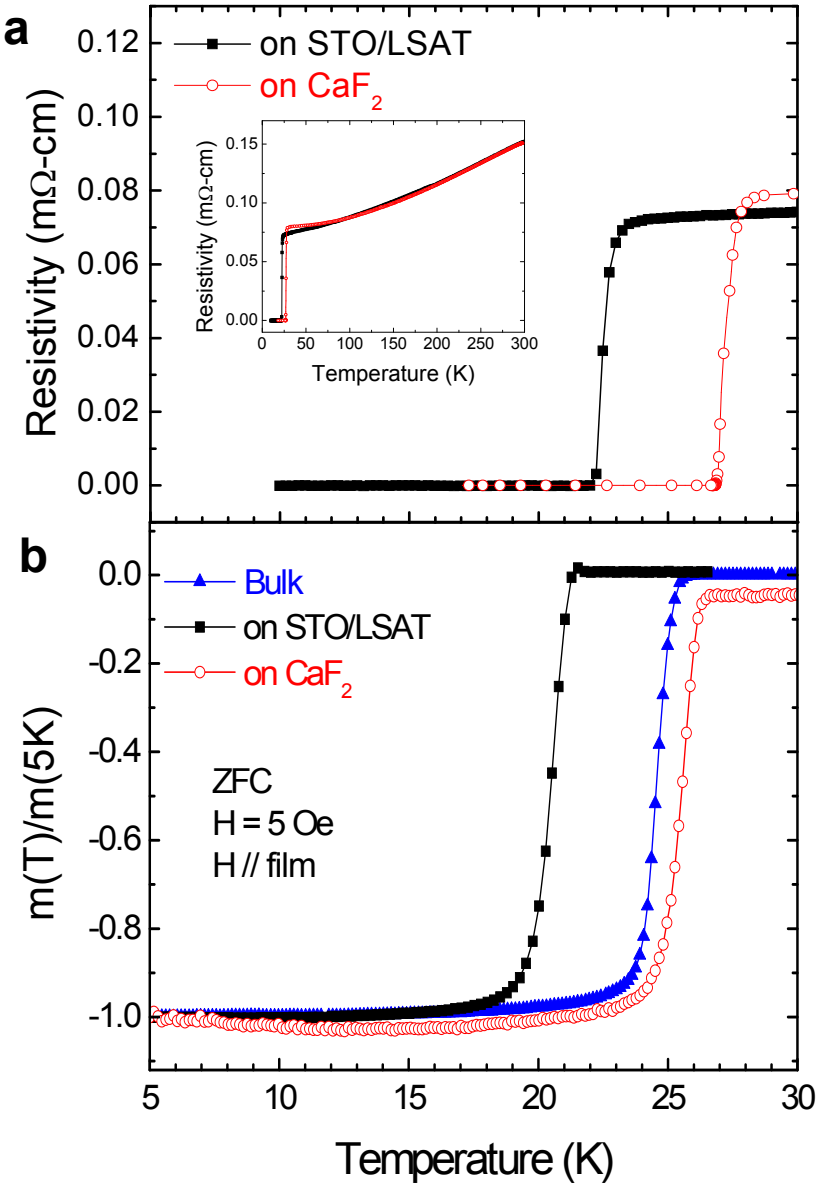

Figure VI.3. Superconducting Transition temperature determined by both a) transport and b) magnetization measurement

As shown in Fig. VI.3a, the film grown on STO/LSAT shows sharp transition and $T_{c,\,\rho=0}$ of

~22K similar with the value previously reported by us [21], in contrast, the films grown on CaF_2 shows dramatically increased and highest ever $T_{c,\rho=0}$ of 26.7K among the Ba-122 thin film and bulk at atmospheric pressure.

Furthermore, we also confirmed it by zero-filed-cooled magnetization T_c transition measurement including bulk polycrystal which was used as the PLD target to grow thin films. As shown in Fig. VI.3b, all three samples have a sharp transition, which means that all samples are homogeneous. The magnetization T_c of both films is almost same as transport $T_{c,\rho=0}$ and we could directly compare the T_c of thin film and the bulk polycrystal. Clearly the T_c of film grown on CaF_2 is higher than that of bulk polycrystal by ~1K, as shown in Fig. VI.3b.

Figure VI.4 shows J_c as a function of magnetic field for both films determined from vibrating sample magnetometer measurements in fields up to 14 T. Both films show high J_c, over 4 MA/cm^2 (4.2K, self filed), which are comparable with the value previously reported and it confirms our strained thin films grown on CaF_2 not only have superior T_c but also could be considerable to be used for the thin film device of high field applications.

To confirm the relationship between T_c and thermal expansion mismatch, we grew Co-doped Ba-122 on BaF_2 ($\alpha = 20 \times 10^{-6}$ /K at 300K) and measured the transport $T_{c,\rho=0}$. Although the crystalline quality of the film on BaF_2 is compromised due to huge lattice mismatch (+9.5%), surprisingly, the $T_{c,\rho=0}$ of the film was higher than that of the film grown on STO/LSAT by 2.7K. Furthermore, the film has compressive strain which is the opposite direction considering the lattice mismatch. So the strain is due to not lattice mismatch but thermal expansion mismatch. To rule out chemical effect of substrate, we

also checked the transport $T_{c,\rho=0}$ of the film grown on STO/CaF_2 and it also shows higher $T_{c,\rho=0}$ than the film on STO/LSAT by 2K (All data is shown in Table VI.1 and Fig VI.5). All the above results show that the thermal expansion mismatch is the key to increase T_c by applying compressive strain in the Co-doped Ba-122 eptiaxial thin films.

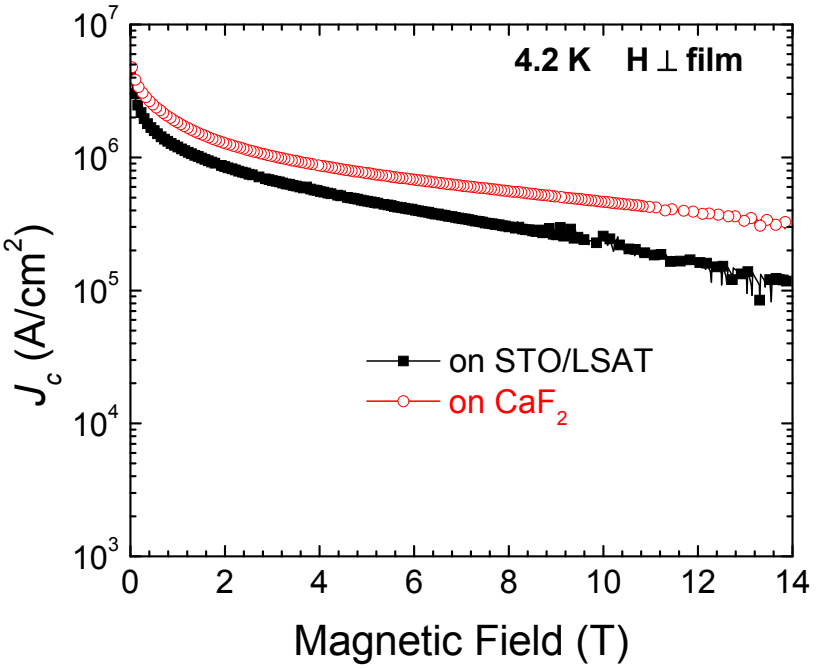

Figure VI.4. J_c as a function of magnetic field of the Co-doped Ba-122 films grown on STO/LSAT and CaF_2

Table VI.1. Crystalline quality and superconducting properties of the Ba-122 films grown on STO/LSAT, CaF_2, BaF_2, and STO/CaF_2. As a reference, bulk single or poly crystal properties are also shown at the right column. FWHM of Rocking curve of Ba-122 (004) reflection, $\Delta\phi$ of 112 off-axis azimuthal ϕ scan are shown to compare crystalline quality. T_c,

$\rho=0$, ΔT_c, and J_c characterize the superconducting properties.

Co-doped Ba122 thin films on	STO/LSAT	CaF_2	BaF_2	STO/CaF_2	Single or poly crystal Co-doped Ba122
Lattice mismatch (%)	-2.6	-2.6	+9.5	-2.6	
a=b direction Thermal expansion coefficient at 300K (X 10^{-6}K)	10	18.7	20	18.7	8
a lattice (Å)	3.963	3.933	3.935	3.936	3.964
c lattice (Å)	12.965	13.090	13.064	13.067	12.980
FWHM $\Delta\omega$ (º)	0.34	0.49	2.50	0.75	
FWHM $\Delta\phi$ (º)	0.77	0.58	4.60	0.78	
$T_{c,\rho=0}$ (K)	22.0	26.7	24.7	23.9	25.8
ΔT_c (K)	0.8	1.0	2.0	3.1	
J_c (4.2K, SF) (A/cm^2)	4.0X10^6	5.2X10^6			

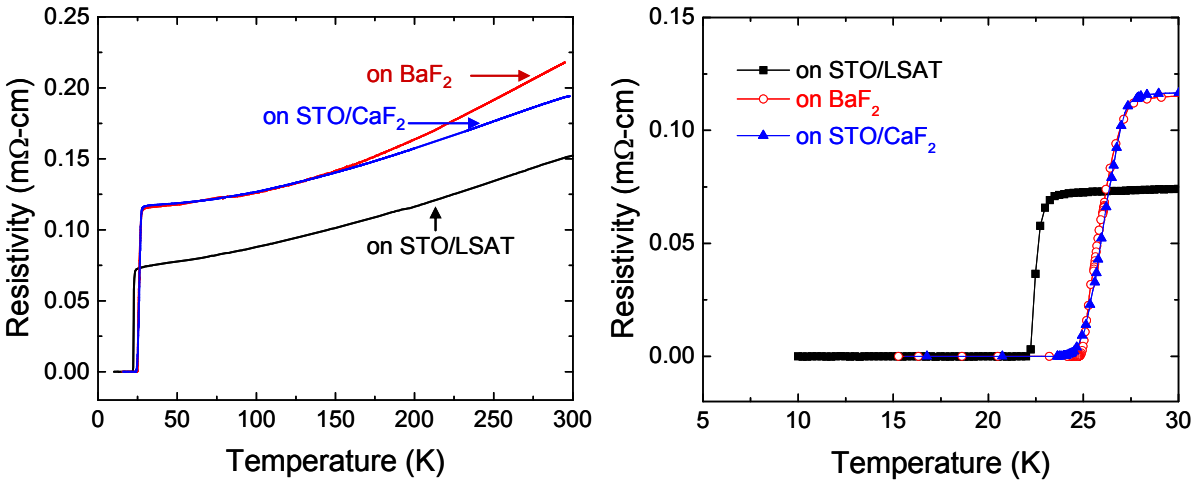

Figure VI.5. Superconducting Transition temperature of the film grown on STO/LSAT, BaF_2, and STO/CaF_2

VI-4. Summary of the chapter

In summary, we show Co-doped Ba-122 thin film which has highest T_c ever using thermal expansion mismatch engineering. The CaF_2 substrate which has high thermal expansion mismatch with Ba-122 was used and it led to the compressive strain in the film. The $T_{c,\ \rho=0}$ of strained films is as high as 26.7K which is even higher than the bulk polycrystal which was used to grow this thin film as the PLD target. Not only T_c, but also crystalline structure and J_c properties of our strained thin film were superior. Furthermore, we believe that the thermal expansion mismatch engineering could be applied to other FeSC phases to increase T_c.

References

[1] Y. Kamihara *et al*., *J. Am, Chem. Soc*. **130**, 3296 (2008).

[2] X. H. Chen *et al*., *Nature* **453**, 761 (2008).

[3] C. Wang *et al*., *Euro Phys. Lett*., **83,** 67006 (2008).

[4] M. Rotter *et al*., *Phys. Rev. Lett*. **101,** 107006 (2008).

[5] A. S. Sefat *et al*., *Phys. Rev. Lett*. **101,** 117004 (2008).

[6] F.-C. Hsu *et al*., *Proc. Natl. Acad. Sci. USA* **105,** 14262 (2008).

[7] S. Lee *et al., Appl. Phys. Lett.* **95**, 212505 (2009).

[8] S. Schmidt *et al.*, *Appl. Phys. Lett.* **97**, 172504 (2010).

[9] S. Baily *et al., Phys. Rev. Lett.* **102**, 117004 (2009).

[10] T. Katase *et al.*, *Appl. Phys. Lett.* **96**, 142507 (2010).

[11] M. Mehta *et al., Appl. Phys. Lett.* **97**, 012503 (2010).

[12] A. Perucchi *et al.*, *EPJ B* **77**, 25–30 (2010).

[13] G. Sheet *et al., Phys. Rev. Lett.* **105**, 167003 (2010).

[14] R. V. Aguilar *et al., Phys. Rev. B* **82**, 180514 (2010).

[15] J. Yong *et al., Phys. Rev. B* **83**, 104510 (2011).

[16] M. S. Torikachvili *et al.*, *Phys. Rev. Lett.* **101**, 057006 (2008).

[17] S. A. J. Kimber *et al.*, *Nature Mater.* **8**, 471–475 (2009).

[18] A. S. Sefat, *Rep. Prog. Phys.* **74**, 124502 (2011).

[19] K. Ahilan *et al., Phys. Rev. B* **79**, 214520 (2009).

[20] K. Ahilan *et al,. Journal of Physics: Condensed Matter* **20**, 472201 (2008).

[21] S. Lee *et al*., *Nature Mater.* **9,** 397 (2010).

[22] T. Katase *et al.*, *Appl. Phys. Express* **3**, 063101 (2011).

[23] S. Haindl *et al.*, *Phys. Rev. Lett.* **104**, 077001 (2010).

[24] T. Thersleff *et al., Appl. Phys. Lett.* **97**, 022506 (2010).

[25] T. Kawaguchi *et al., Appl. Phys. Lett.* **97**, 042509 (2010).

[26] I. Tsukada *et al., Appl. Phys. Express* **4**, 053101 (2011).

[27] K. Iida *et al., Appl. Phys. Lett.* **97**, 172507 (2010).

[28] T. Katase *et al., Nat. Commun.* **2**, 409 (2011).

[29] K. Iida *et al*., *Appl. Phys. Lett*. **95,** 192501 (2009).

[30] S. Ueda *et al*., *Appl. Phys. Express* **99**, 232505 (2011).

[31] E. Bellingeri *et al., Appl. Phys. Lett.* **96**, 102512 (2010).

[32] M. S. da Luz *et al., Phys. Rev. B* **79**, 214505 (2009).

Chapter VII. Summary

The purpose of this thesis work is the growth of genuine Co-doped Ba-122 superconductor thin films, study about its grain boundaries properties, and tailoring of its superconducting properties by demonstration of artificial layered superlattices and a strain effect.

VII-1. Growth of genuine epitaxial Co-doped Ba-122 thin film and its properties of grain boundaries

To turn granular, low critical current density superconducting films grown on various pervskite substrates into single crystal like high-J_c, and genuine epitaxial Co-doped Ba-122 thin films, we have developed a novel template engineering technique which could favor bonding between the Ba alkaline-earth component of the pnictide phase and the underlying oxide substrate by using template engineering with the intermediate STO or BTO layers. J_c in our high-quality epitaxial films grown by template engineering is about 10 times greater than in bulk single crystals and ~400 times greater than in previously reported AE-122 films. Not only on perovskite substrate but also on semiconductor substrate Si, we could grow genuine high quality epitaxial Co-doped Ba-122 film. Indeed thin film grown on epitaxial STO-template / (001) Si substrates shows $T_{c,\rho=0}$ = 18 K, ΔT_c = 1K without any misoriented grains. This approach thus greatly expands substrate choices for high-quality Ba-122 thin films, thus allowing much broader fundamental property investigations of the newly discovered ferropnictide superconductors and parent

compounds, as well as for exploring their applications. Furthermore, we expect that epitaxial thin films of other layered intermetallics could be successfully grown on various types of oxide substrates by employing similar template engineering principles.

Our results about grain boundaries (GB) of Co-doped Ba-122 show that uncovering the fundamental mechanisms that induce GB weak links is vital, since pnictides are only the second class of superconductors with T_c greater than 50 K. Since the qualitative mechanisms of GB weak link behavior discussed in chapter IV are rather insensitive to details of their pairing scenarios and superconducting order parameter symmetry, we suggest that conditions favorable for weak linked GBs will be present in any high-T_c superconductor with competing orders, short coherence length and low carrier density. Given how deleterious GB current-blocking effects have been to applications of the cuprates, it is indeed very important to understand in much greater detail how GBs change from being beneficial pinning centers in the low T_c metallic superconductors like Nb_3Sn and $SnMo_6S_8$ to weak links in these high T_c doped superconductors. Ongoing quests for new high-T_c (or even room temperature) superconductors should therefore also focus on their sensitivity to structural disorder, especially that which occurs at grain boundaries.

VII-2. Tailoring superconducting properties by artificial layered superlattices and a strain effect

We have demonstrated successful growth of epitaxial Co-doped Ba-122 pnictide superlattices with controlled structural and compositional modulations. As an application

of such model structures, we show simultaneous control of defect structure both in the interface region and along *c*-axis direction by varying suitable interlayer compositions and materials. These optimized defects contribute towards effective pinning over wide angular range leading to strong increase in J_c and H_{irr} as compared to single layer thin films. In particular, O-Ba-122 insertion layer could promote formation of *ab*-axis aligned second phase nano particles without prohibiting the formation of vertically aligned defects. In such engineered structures, we could achieve irreversibility field higher than 45 Tesla (T=4.2 K, H|//*ab* plane) and critical current density above 2×10^5 A/cm^2 (T=4.2 K, H//*ab* = 20 T). Such superlattice structure is a first step towards achieving isotropic J_c enhancement in pnictide thin films by optimizing interlayer separation and oxygen content at the defect sites. The success in growth of such high quality artificially layered structure will have wider implication towards achieving new interface driven high T_c superconductivity and potential device applications involving SNS junctions.

We also investigated a strain effect on T_c of Co-doped Ba-122 by using CaF_2 substrate which has large thermal expansion mismatch with Co-doped Ba-122. It turns out Co-doped Ba-122 thin film grown on CaF_2 substrate shows highest T_c ever. Grown Co-doped Ba-122 epitaxial thin films shows highly compressive strained state and the $T_{c,\,\rho=0}$ of strained films is as high as 26.7K which is even higher than the bulk polycrystal. In addition, crystalline quality and J_c of our strained thin film are also superior. We believe that the thermal expansion mismatch approach could be applied to other FeSC phases to tailor their T_c.

APPENDIX ; Dependence of epitaxial Co-doped $BaFe_2As_2$ thin films properties on $SrTiO_3$ template thickness

There is great interest in studying the intrinsic properties and technological applications of the newly discovered iron pnictide superconductor [1]-[4]. High-quality epitaxial pnictide thin films are inevitable, but the growth of epitaxial thin films with superior superconducting properties has been hard to produce, especially the F-doped highest T_c rare-earth 1111 phase [5]-[8]. As the dopant, F, is volatile at growth temperature it has been very difficult to control the stoichiometry of the . rare-earth 1111 thin films. In contrast, $Ba(Fe_{1-x}Co_X)_2As_2$ (Ba-122) is comparatively suitable for growing thin film using low vapor pressure element Co as a dopant. Epitaxial growth of Ba-122 thin films was reported by us and other groups [9]-[18]. The Ba-122, $SrTiO_3$ (STO), and $BaTiO_3$ (BTO) has divalent alkaline-earth (AE) elements on the same lattice sites, while other perovskite oxides such as (La, Sr)(Al, Ta)O_3 (LSAT) or $LaAlO_3$ (LAO) have a trivalent element. Building upon this common feature, we grew high quality Co-doped Ba-122 epitaxial thin films on (001)-oriented STO bicrystal substrates [17]. However, the STO substrates became electrically conducting during deposition of the Co-doped Ba-122 thin film at 750^{o}C in the high vacuum (~10^{-6} Torr), owing to formation of oxygen vacancies in the STO [19]. This provides a parallel, current-sharing path between Ba-122 and STO, which compromises normal-state property studies. By employing either an STO or BTO template on various perovskite substrates, we could have demonstrated the growth of genuine epitaxial Ba-122 thin films on non-conducting substrate with the superior crystalline and superconducting properties [18]. We found that the STO or BTO template is critical for growing epitaxial

Ba-122 in our growth condition. In this appendix, we show the dependence of the properties of Ba-122 thin films on the STO template thickness. According to the result, a minimum thickness is needed to suppress the formation of in-plane misoriented grains. We have also found that there is an optimum thickness of templates to obtain the best structural and superconducting properties of Ba-122 thin films.

Epitaxial STO thin film templates were grown on (001) LSAT substrates at 750 °C , in 8 mTorr of oxygen atmosphere by pulse laser deposition (PLD) with high-pressure reflection high-energy electron diffraction (RHEED) for digital control [20] and *in situ* monitoring of the growth. The thicknesses of the STO templates we studied were 2, 20, 50, 100, and 150 unit cells (u.c.). We measured the surface roughness and crystalline quality of STO templates as a function of the STO thickness with atomic force microscopy (AFM) and x-ray diffraction (XRD), respectively. For all films, the root mean square (RMS) values measured with AFM are about 0.2 nm, which means the surface roughness is the same regardless of the template thickness (the AFM image is not shown here). All STO templates are perfect single crystalline with extremely sharp rocking curves (the full width at half maximum (FWHM) values (about 0.016^{o}) of the rocking curve for the STO 002 reflections). Note: We were not able to determine the crystalline quality of 2 u.c. STO because it is too thin to be measured with XRD. Figure A.1 shows the 002 rocking curve scans of 100 and 150-u.c.-thick STO templates (20 u.c. and 50 u.c. STO are not shown here, but the shape is the same as 100 u.c. STO). Although the FWHM is comparable for both films, there are shoulders (satellite peaks) at both sides of the main peak for 150 u.c. STO, due to threading dislocations and strain relaxation. This means that the STO templates are fully coherent to the LSAT substrates up to 100 u.c. STO. On top of these STO templates, 350-nm-thick Ba-

122 thin films were grown with PLD in vacuum at 750 °C. The detailed growth conditions were reported elsewhere [18]. The Ba-122 targets were prepared with a solid-state reaction with a nominal composition of Ba/Fe/Co/As = 1:1:84:0:16:2:2. Based on the result of wave dispersive X-ray spectroscopy, the typical composition of our Ba-122 thin film was Ba /Fe/Co/As/O = 1:1.7:0.13:1.7:0.3. The structural and superconducting properties of Ba-122 thin films are listed in Table 1.

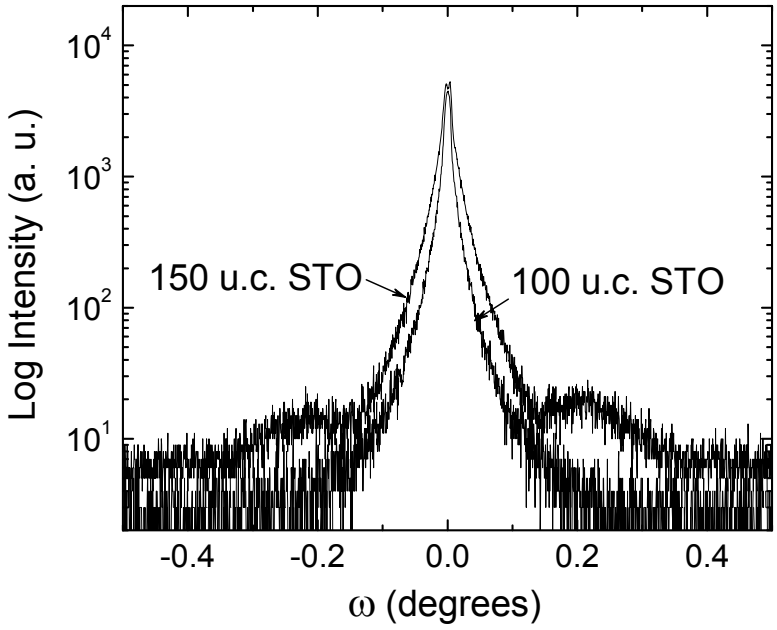

Figure A.1. XRD Rocking curves of 002 reflection for 100 and 150 u.c. thick STO templates

TABLE A.1 Crystalline quality and superconducting properties of Ba-122 thin films

	Ba-122/STO templates/LSAT				
Template thickness	2 u.c.	20 u.c.	50 u.c.	**100 u.c.**	150 u.c.
FWHM $\Delta\omega$ of 004 reflection	1.45	0.96	0.84	**0.55**	0.84
FWHM $\Delta\phi$ of off-axis 112 reflection	2.71	1.65	0.98	**0.8**	0.97
Extra peaks in ϕ scan	Yes	Yes	**No**	**No**	**No**
$T_{C,\ onset}$ (K)	18.9	20.5	20.7	**22.8**	21.6
ΔT (K)	n/a	4.2	1.2	**1.3**	1.6
J_c (4.2K, Self field) (A/cm^2)	2.3×10^4	5.6×10^5	1.7×10^6	$\mathbf{2.9\times10^6}$	2.2×10^6

The template thickness dependence of the crystalline quality and the epitaxial arrangement of Ba-122 thin films were determined with four-circle XRD. Figure. A.2 (a) shows θ-2θ scans of the Ba-122 grown on the 100 u.c. STO/LSAT. The XRD pattern shows that the film 00*l* reflections dominate, which indicates *c*-axis growth normal to the STO template and the LSAT substrate. Ba-122 films on different STO thicknesses have the same out-of-plane texture (not shown here) although the intensity of the Ba-122 00*l* peaks is weaker at Ba-122 on thinner STO templates. An extra peak at $2\theta = \sim 65^o$ is identified as 002 reflection of Fe although the intensity is less than 5% of the 004 reflection of the Ba-122 peak.

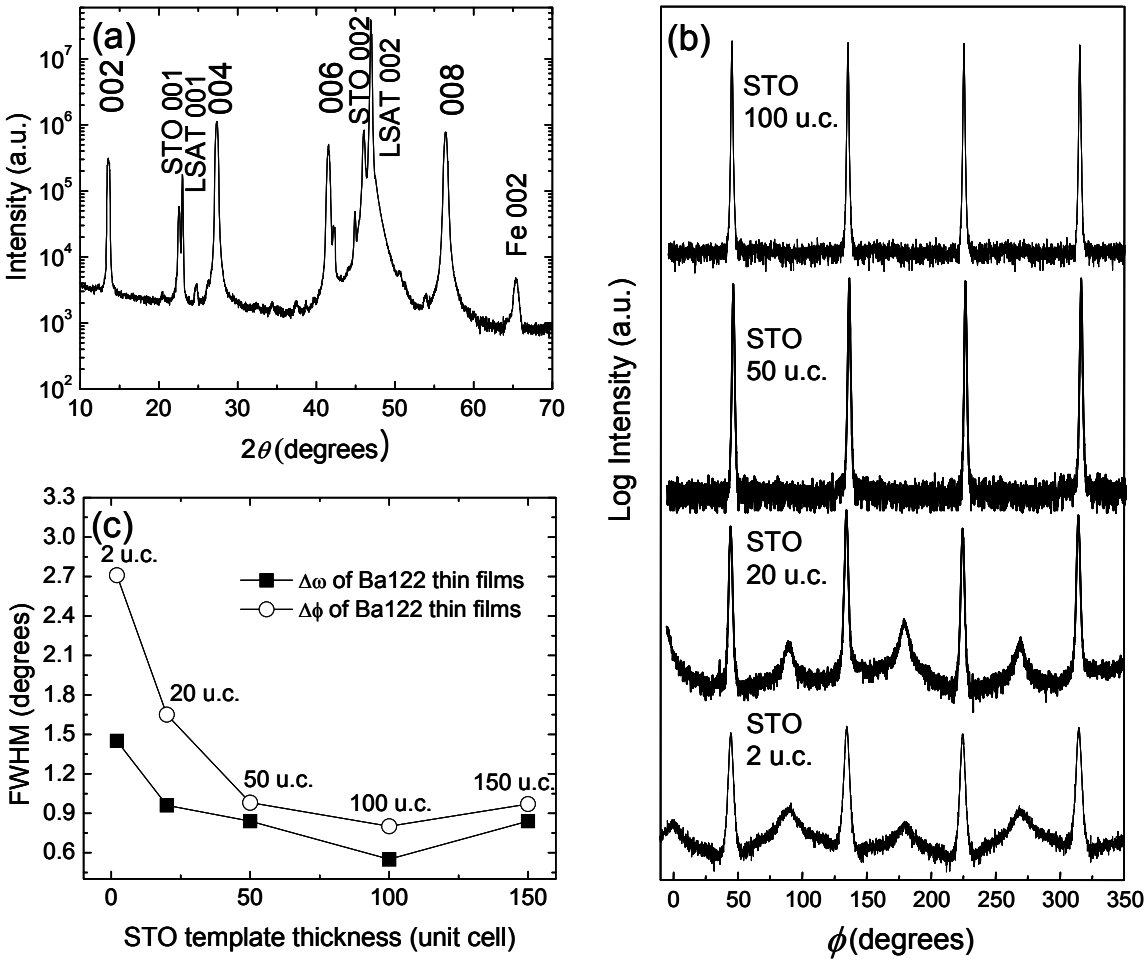

Figure A.2. XRD analysis of Ba-122 films (a) out-of-plane XRD pattern of Ba-122/100 u.c. STO/LSAT. All non-identified peaks are reflections of identified peaks resulting from CuKβ and CuKα+β. (b) azimuthal ϕ scan of the off-axis 112 reflections for Ba-122/2, 20, 50, 100 u.c. STO/LSAT (c) FWHM $\Delta\omega$ of 002 and $\Delta\phi$ of the off-axis 112 reflections for all Ba-122 films

The in-plane texture of Ba-122 was determined with azimuthal ϕ scans of the off-

axis 112 peak, as shown in Fig. A.2 (b). The films grown on the 2 and 20 u.c. STO templates on the LSAT substrates exhibit extra peaks at intermediate ϕ angles in addition to the major peaks at every 90°. This indicates that the Ba-122 films contain misoriented grains in the plane with 001 tilt high-angle grain boundaries [18]. In contrast, the films on the 50, 100 and 150 u.c. thick STO on the LSAT substrate show only strong peaks at every 90°, which indicates that these films have a genuine epitaxial arrangement in the plane (150 u.c. is not shown here).

We determined the out-of-plane and in-plane mosaic spreads and crystalline quality of the films by performing rocking curve and azimuthal ϕ-scans, respectively. Figure A.2 (c) shows the FWHM values of the 004 rocking curve ($\Delta\omega$) and $\Delta\phi$ of the Ba-122 as a function of the STO template thickness. Both the FHWM $\Delta\omega$ and $\Delta\phi$ values rapidly decreased from 2 u.c. to 50 u.c. as the STO thickness increased and reached the minimum at the STO thickness of 100 u.c. This trend is consistent with the in-plane texture and the absence of misoriented Ba-122 grains at an STO thickness above 50 u.c. as shown in Fig. A.2 (b). We can make three conclusions from the XRD data. First, a minimum template thickness of 50 u.c. STO is needed to obtain genuine epitaxy. Second, the optimum template thickness is 100 u.c. Finally, the high crystalline quality of Ba-122 is maintained above the minimum templates thickness (about 50 u.c.) but slightly compromised above the optimum thickness (about 100 u.c.). This might be due to the compromised STO template quality with surface defects, threading dislocation, and strain relaxation above 100 u.c. as shown in Fig. A.1.

The superconducting transition temperature (T_c) and transition width (ΔT_c) were

determined by a resistivity measurement. The resistivity of the films with a size of about 2 mm x 4 mm was measured in a Quantum Design PPMS by a four-point probe method with the current flow along the sample length direction. As shown in Fig. A.3 (a), the film grown on 20, 50, 100, and 150 u.c. STO shows a residual resistivity ratio (about 1.9) similar to that of the Ba-122 bulk single crystal [21]. However, as shown in Fig. A.3 (b), the film on 20 u.c. STO shows a double transition, which is due to the non-homogeneous superconducting phases. All other films with thickness above 50 u.c. show narrow transition width. As listed in Table 1 and Fig. A.3 (b), both the on-set T_c ($T_{c,\ on\text{-}set}$) and ΔT_c are improved from 2 u.c. STO to 100 u.c STO and degraded 100 u.c. STO to 150 u.c. STO, which is clearly consistent with the trend of crystalline structure properties. Especially, the film grown on the optimum template thickness (100 u.c. STO) shows the highest $T_{c,\ on\text{-}set}$ of 22.8 K with almost the narrowest ΔT_c of 1.3 K.

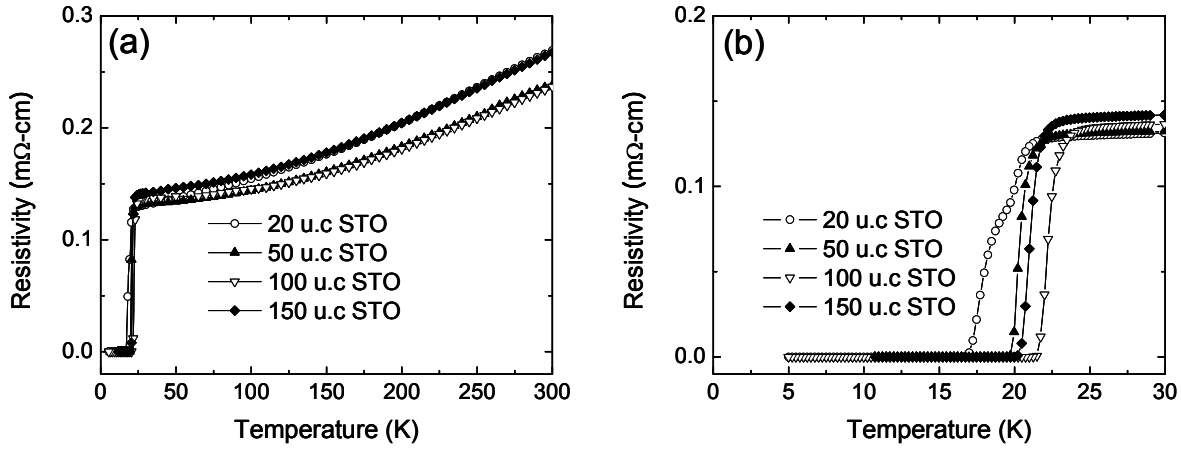

Figure A.3. Resistivity as a function of temperature for the Ba-122 thin films grown on 20, 50, 100, and 150 u.c. STO templates

Figure A.4 shows the zero-field-cooled magnetization T_c transitions of Ba-122 thin films grown on 20, 50, 100, and 150 u.c. STO templates on the LSAT substrate. All films have a similar strong diamagnetic signal except the film grown on the 20 u.c. STO template, which clearly shows granularity associated with the inability of screening currents to develop across the high-angle grain boundaries in the film on the 20 u.c. STO/LSAT. In contrast, the film grown on the 100 u.c. STO/LSAT shows a strong signal and the highest magnetization T_c, which is consistent with the result of the resistivity T_c measurement.

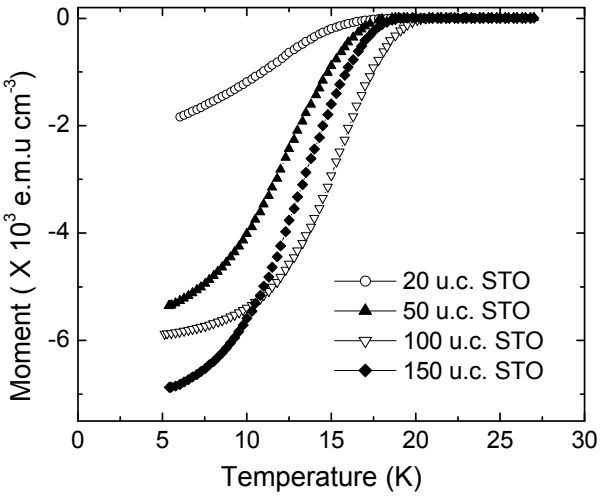

Figure A.4. Magnetic moment as a function of temperature for Ba-122 grown on 20, 50, 100, and 150 u.c. STO templates

Figure A.5 shows the critical current density (J_c) vs. the applied magnetic field for Ba-122 films grown on 20, 50, 100, and 150 u.c. STO templates measured with a vibrating sample magnetometer up to 14 T. Magnetization as a function of temperature of the

samples was measured by a Quantum Design SQUID magnetometer with a field of 2 mT perpendicular to the film surface. The magnetization loop of the films with a size of about 2 mm x 4 mm was measured in a 14 T Oxford vibrating sample magnetometer (VSM) at 4.2K with the applied field perpendicular to the film surface. Magneto-optical imaging was used to examine the uniformity of current flow in the films so as to validate the use of the Bean model for converting the magnetic moment measured in the VSM to J_c assuming current circulation across the whole sample without granular effects. For a thin film, J_c = 15Δm/(V r), where Δm is the width of the hysteresis loop in emu, V the film volume in cm^3, and r the radius corresponding to the total area of the sample size, and was calculated from πr^2 = a x b (a and b are the film width and length in cm, respectively). Here all films show higher J_c than that of bulk single crystal (0.4 MA/cm^2 at 4.2 K; ref. [22]). Furthermore, the J_c of the epitaxial films on the 100 and 150 u.c. STO shows a weak field dependence, indicative of little or no suppression of the J_c by strong magnetic fields. Those films had J_c up to about 0.4 MA/cm^2 even at 13 T. According to transmission electron microscopy (TEM) analysis, this is due to the second-phase self-assembled nano-pillars in the Ba-122 matrix, which could act as a very effective pinning center as shown in our previous report [23]. However, the films on the 50, 100, and 150 u.c. STO template have much higher J_c than the film on the 20 u.c. STO by a factor of 5. We believe this is due to the superior epitaxial arrangement in Ba-122 on thicker STO templates (above 50 u.c.) as confirmed by XRD analysis, while the films on the 2 and 20 u.c. STO template have a high-angle grain boundary within the in-plane structure. According to our previous report [17], [001] Ba-122 on STO bicrystal substrates with θ = 6°–24° misorientation angles show significant

suppression of the J_c. It does make sense that randomly oriented high-angle tilt grain boundaries in the Ba-122 on thinner templates (2 and 20 uc) would effectively block the supercurrent, as suggested by several recent pnictide film reports [5]-[11].

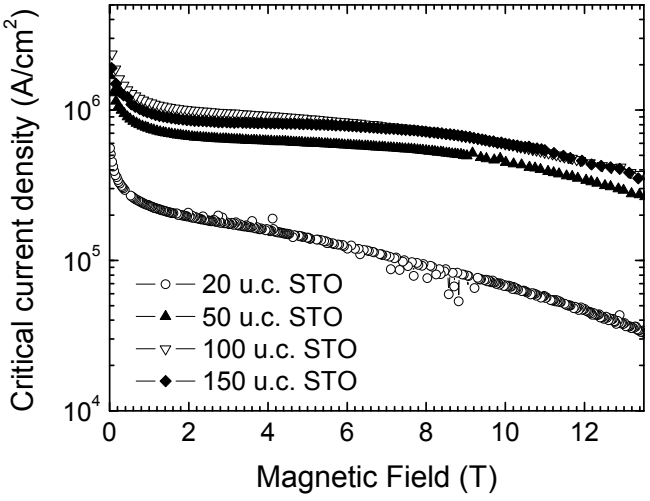

Figure A.5. Critical current density as a function of applied magnetic field at 4.2K for Ba-122 grown on 20, 50, 100, 150 u.c. STO templates

Compared with the Ba-122 thin films grown on the bare LSAT, the films grown on even the 2 u.c. STO template on the LSAT substrate was significantly improved in terms of crystalline quality, which indicates that the template itself is critical for growing Ba-122 thin films. However, as shown so far, at least about a 50 u.c. template is needed to grow genuine epitaxial Ba-122 thin films without any misoriented grains. According to recent reports, an epitaxial Fe layer was formed between Ba-122 and the LSAT substrate for Ba-122 films grown at ultra-high vacuum (UHV) (about 10^{-8} Torr) [13]-[14]. This indicates

highly reactive Ba and As diffuses into the LSAT substrate and forms the epitaxial Fe layer at the interface. We also found some localized disorder of the atomic arrangement at the interface between Ba-122 and the STO template revealed by transmission electron microscopy (TEM) [18]. This disorder might be evidence of interdiffusion between Ba-122 and substrate films grown at our growth condition (~ 10^{-6} torr). We believe a thicker STO template provides an effective diffusion barrier between Ba-122 and the LSAT substrate so that the epitaxial growth of Ba-122 is maintained throughout the growth of Ba-122 films. We believe that about 50 u.c. is the minimum thickness for an effective diffusion barrier in our growth condition. Beyond the optimum template thickness of 100 u.c., the quality of Ba-122 is slightly reduced. We believe this is due to various defects generated by strain relaxation of STO templates.

We studied the influence of a single crystalline STO template thickness on the properties of epitaxial Ba-122 thin films in the thickness range of 2–150 u.c. STO on (001) LSAT substrates. We obtained genuine epitaxial Ba-122 thin films on STO templates for thicknesses above 50 u.c. in our Ba-122 growth conditions. We believe that a minimum STO thickness is needed to effectively block interdiffusion between Ba-122 and the STO template during the growth of Ba-122 thin films. We have obtained Ba-122 films with the best crystalline quality and superconducting properties quality at the optimum 100 u.c. STO in which the STO template is the largest thickness with coherence to the LSAT substrate. Beyond the optimum STO thickness, the crystalline property of Ba-122 is slightly degraded owing to compromised STO crystalline quality due to surface defects, threading dislocation, and strain relaxation of STO templates.

References

[1] Y. Kamihara et al., *J. Am. Chem. Soc.* 130, 3296 (2008).

[2] X. H. Chen *et al*., *Nature* **453**, 761 (2008).

[3] C. Wang *et al*., *Euro Phys. Lett*., **83,** 67006 (2008).

[4] M. Rotter *et al*., *Phys. Rev. Lett*. **101,** 107006 (2008).

[5] H. Hiramatsu *et al*., *Appl. Phys. Lett*. **93,** 162504 (2008).

[6] S. Haindl *et al*., *Phys. Rev. Lett*. **104,** 077001 (2010).

[7] M. Kidszun *et al*., *Supercond. Sci. Tech*. **23** 022002 (2010).

[8] M. Kidszun *et al*., *Europhys. Lett*., **90** 57005 (2010).

[9] H. Hiramatsu *et al*., *Applied Physics Express* 1, 101702 (2008).

[10] T. Katase *et al*., *Solid State Communications* 149, 2121 (2009).

[11] E. M. Choi *et al*., *Appl. Phys. Lett.* 95, 062507 (2009).

[12] K. Iida *et al*., *Appl. Phys. Lett*. **95,** 192501 (2009).

[13] K. Iida *et al*., *Phys. Rev. B.* **81** 100507 (2010).

[14] T. Thersleff *et al*., *Appl. Phys. Lett.*, **97** 3457432 (2010).

[15] T. Katase *et al.*, *Appl. Phys. Lett.* **96**, 142507 (2010).

[16] T. Katase *et al., Appl. Phys. Express* **3**, 063101 (2010).

[17] S. Lee *et al., Appl. Phys. Lett.* **95**, 212505 (2009).

[18] S. Lee *et al*., *Nature Mater.* **9,** 397 (2010).

[19] G. Herranz *et al*., *Phys. Rev. Lett.* **98,** 216803 (2007).

[20] G. J. H. M. Rijnders *et al*., *Appl. Phys. Lett.* **70** 1888 (1997).

[21] A. S. Sefat *et al*., *Phys. Rev. Lett*. **101,** 117004 (2008).

[22] A. Yamamoto *et al.*, *Appl. Phys. Lett.* **94,** 062511 (2009).

[23] C. Tarantini *et al. Appl. Phys. Lett*. **96**, 142510 (2010).

Acknowledgement

I would like to thank my advisor, Prof. Chang-Beom Eom, for excellent guidance, encouragement and support. It was fortune to have an advisor like him, who endlessly cared about my work and encourage me to find interesting scientific issue. Also, I would like to thank my committee members for their guidance.

It was lucky for me to meet passionate researchers like Oxide group members. I would like to thank them. Also, I would like to thank Prof. David Larbalestier, Prof. Eric Hellstrom in Florida State University, Prof. Xiaoqing Pan in University of Michigan, and their all group members for our excellent collaboration.

I must express my gratitude to my wife, Jimi, for her prayer and support during my long journey. Especially, my little son, Daniel was a source of constant delight and cheered me up whenever I was exhausted. Also, I would like to thank my parent for their endless support and prayer every early morning for me.

Finally I would like to thank God because I know I could not finish this work without him.